Time Domain Principal Component Analysis for Rapid, Real-Time 2D MRI Reconstruction from Undersampled Data

by

Mark Geoffrey Wright

A thesis submitted in partial fulfillment of the requirements for the degree of

Master of Science

in

Medical Physics

Department of Oncology
University of Alberta

Abstract

Hybrid Linac-MR systems are becoming more mainstream for use in external beam radiotherapy treatments for cancer patients. The addition of an MR scanner to a linear accelerator (Linac) can allow for real-time structure tracking (such as a tumour) and on-the-fly adjustments of the radiation beam. This will allow for smaller treatment margins meaning more healthy tissue will be spared from irradiation. While MR provides superior soft-tissue contrast compared to other modalities, typical methods used are computationally expensive and require complicated setups or are otherwise too slow for real-time applications.

The work proposed here utilizes a sliding window, Principal Component Analysis (PCA) in the temporal domain along with undersampled data from previously acquired frames in the sliding window to fully reconstruct the final frame within this window. Data is acquired such that a core set of phase encodes, located in central k-space, is acquired in every frame. PCA is performed on this data in order to characterize the temporal change in k-space. Outside of this core, the outer k-space is acquired in such a way that all of k-space is covered within a pre-determined number of frames. The principal components, which are continuously updated over an imaging session, are combined with the undersampled data to calculate weights which are used with the acquired data of the frame of interest to fill in the missing data.

The method was tested retrospectively on 15 fully-sampled data sets of lung cancer patients acquired on a 3T MR scanner. A subset of six data sets was tested to determine the ability to contour a structure on the reconstructed images. The contours were developed using auto-contouring software and compared to contours developed on the original fully-sampled data sets.

Due to changes in signal-to-noise ratio found at different MR field strengths, the algorithm was tested to determine the effects of added noise. Six data sets were used to retrospectively test the algorithm at noise levels of 2, 4 and 6 times greater than those calculated on the original 3T data. The reconstructed images were again tested for overall image quality as well as the ability to contour a structure on the reconstructed images.

Previous work has utilized PCA corresponding to the spatial domain (intra-frame PCA method) to reconstruct images. The principal components were calculated from a database of fully-sampled images acquired just before the treatment. Initially the method worked very well, however as the imaging session progressed, image quality and contour metrics showed deterioration. Comparisons were made between this method and the one proposed in this work in order to test the robustness of the method. While the intra-frame method appeared to perform better initially, the through frame method maintained consistent metrics throughout an imaging session and performed better as time went on. This through frame PCA method appears to remain robust even at high acceleration rate and low SNR values.

Preface

All lung tumour image data were acquired under local ethics board approval and were used under collaboration with the investigators. The auto-contouring software used in this work was developed by Dr. Jihyun Yun and used with his permission. Technical aspects of the code are discussed in the first author paper:

Yun, J., Yip, E., Gabos, Z., Wachowicz, K., Rathee, S., Fallone, B. G. Neural-network based autocontouring algorithm for intrafractional lung-tumor tracking using Linac-MR. Med Phys, 2015;42(5):2296-2310.

The code for the intra-frame PCA method was developed by Dr. Bryson Dietz and used with his permission which is discussed in the first authored paper:

Dietz, B., Yip, E., Yun, J., Fallone, B. G., Wachowicz, K. Real-time dynamic MR image reconstruction using compressed sensing and principal component analysis (CS-PCA): Demonstration in lung tumor tracking. *Medical Physics*, 2017;44(8):3978-3989.

A version of Chapter 2 and some data from Chapter 3 were published as a first author research article:

Wright M, Dietz B, Yip E, Yun J, Gabos Z, Fallone BG, Wachowicz K. Time Domain Principal Component Analysis for Rapid, Real-Time 2D MRI Reconstruction from Undersampled Data. *Medical Physics*. 2021;48:6724-6739. https://doi.org/10.1002/mp.15238

Acknowledgements

There are many people I would like to thank for their help over the course of the ups and downs of this project.

To my parents Janice and Stuart and sister Stephanie thank you for all your support and encouragement over the course of this degree.

To Dr. Keith Wachowicz, thank you for being an integral part of in making sure this project was a success. Thank you for your invaluable insight, patience, and feedback throughout this entire process.

To Dr. Gino Fallone and Dr. Jay Yun, thank you for being apart of my committee. Thank you for your feedback throughout the manuscript and thesis writing process and for the lively discussion of the project throughout.

To Dr. Alan Wilman thank you for being an arm's length examiner of the project and for your feedback and comments on the thesis.

To Dr. Eugene Yip and Dr. Bryson Dietz, thank you for your feedback and insight throughout the project and the manuscript writing process.

Thank you to the students and staff of the Medical Physics Department and to the staff of the Department of Oncology thank you for your help with courses, labs and navigating the program and answering the many questions I had. Thank you for making the entire journey as enjoyable as possible.

Table of Contents

List of Tables

List of Figures

Chapter 1

Introduction

1.1 Thesis Organization

The focus of this thesis is the use of Principal Component Analysis (PCA) to assist in the reconstruction of undersampled data for use in real-time magnetic resonance imaging (MRI). The goal of this work is to investigate the feasibility of this MRI method for use on hybrid Linac-MR systems. Chapter 1 provides a background into the hybrid Linac-MR system including the components, external beam radiotherapy (EBRT) and MRI. Some motivations for this work and an introduction to PCA are also discussed. Chapter 2 focuses on the development of our method and testing through retrospective analysis on fully-sampled 3T data and the corresponding results. Chapter 3 investigates the effects of added noise on the method. The investigation on the effects of added noise is important due to the increased noise found in MRI at lower field strengths. Chapters 2 and 3 demonstrate the robustness of the proposed method over a range of field strengths. This will allow the method to be applied broadly. Finally, Chapter 4 provides the conclusions drawn from this research and provides suggestions for future work.

1.2 Background

As of 2019 an estimated 1 in 2 Canadians will develop cancer in their lifetime.[1] It is further estimated that 1 in 4 Canadians will die from cancer.[1] Lung cancer is the most prevalent cancer in Canada accounting for 13% of all cancer cases and 26% of all cancer deaths.[1] On top of the physical toll that cancer takes, there is also a large economic burden. One study found that the economic costs of cancer have risen from $2.9 billion in 2005 to $7.5 billion in 2012.[2]

There are three main treatment options when one is diagnosed with cancer and these methods are often combined over the course of a patient's treatment. The methods used in treatment are surgery, chemotherapy, and radiation therapy. The use of each of these treatments is dependent on the location, size, aggressiveness and staging of the tumour. Surgery is used to remove some or the entire tumour depending on its size and location. Surgery can either be done traditionally where a large incision is made in the body or through minimally invasive methods. Surgery often requires the patient to be placed under anesthetic which can produce risks to the patient.[3] Further

side effects of surgery include pain, scarring, infection, and nerve damage amongst others.[3] Chemotherapy is another form of cancer treatment. Chemotherapy involves the use of special drugs designed to kill cancer cells through the uptake of the drugs by the tumour.[4] Some of the common side effects of chemotherapy include nausea and vomiting, loss of appetite, hair loss and fatigue.[4] The third type of cancer treatment is radiation therapy. This can be done internally through brachytherapy or externally through external beam radiation therapy (EBRT). Brachytherapy involves placing radioactive seeds in the body in or near the tumour. High dose rate (HDR) brachytherapy involves a single high dose of radiation delivered within a couple minutes.[5] A patient will typically receive HDR treatment over several days. Low dose rate (LDR) brachytherapy involves a continuous delivery of low dose radiation over several hours.[5] LDR treatment involves the implanting of seeds in or near the tumour on a permanent basis.[5] EBRT involves a machine, most commonly a linear accelerator (LINAC), which develops and directs a beam of radiation towards the tumour.[6] Other types of EBRT include CyberKnife and Gamma Knife.

Typical side effects of radiation therapy include fatigue, skin irritation, hair loss, loss of appetite, nausea and vomiting. More specific side effects are dependent on the site being irradiated. For example, radiation of the brain can lead to temporary cognitive issues, headaches or in certain cases seizures.[6] Other site-specific side effects include dry mouth and difficulty swallowing for head and neck patients, cough or heartburn for chest patients and fertility and bodily functions issues for pelvis patients.[6]

1.3 External Beam Radiation Therapy

EBRT involves the use of high energy (on the order of megavolts) radiation beams. On a LINAC this can be performed in multiple ways including 3D-CRT, IMRT, VMAT, SRS and SBRT.[6] Three-dimensional conformal radiation therapy (3D-CRT) involves creating a 3D visualization of the tumour from CT or MR images. A treatment plan is created which defines beams of the same intensity aimed at the tumour from various angles.[6] Intensity modulated radiation therapy (IMRT) is a more advanced version of 3D-CRT where each of the defined beams have a different intensity.[6] This allows for healthy tissue and organs, for which the beam must pass through to get to the tumour, to receive less dose while increasing the intensity for beams from angles that do not pass through organs. Further to this volumetric-modulated radiation therapy

(VMAT) is a specialized version of IMRT where the radiation is delivered in a continuous 360-degree arc while still modulating the intensity at different angles.[6] These types of radiation therapy are often delivered once a day for several weeks. Stereotactic radiosurgery (SRS) and stereotactic body radiation therapy (SBRT) are highly focused, high intensity beams of radiation.[6] These types of radiation therapy allow for a high dose to the tumour while sparing healthy tissue. SRS and SBRT can be delivered in fewer fractions than standard radiation therapy.[6]

1.3.1 Beam Types

The types of radiation therapy described above use photons as their source of radiation. Photons are the most prominent beam type for radiation therapy clinically in Canada. Photons are produced in a linear accelerator by accelerating electrons in a wave guide which are directed at a metal target; typically, tungsten which then produces high energy photons known as x-rays.[7] The photons produced have a spectrum of energies. Typically, the lower energy photons will be removed before they reach the body using a flattening filter. When the photons reach the body, they will begin to be attenuated. The amount of attenuation will depend on the energy of the photon and the type of material it is passing through i.e., bone or soft tissue. When the photon gets attenuated it interacts with an electron which then travels a short distance before depositing its energy. Attenuation estimations are made from data provided by a CT scan of the region of interest which provides electron density information. Treatments are planned so that most of the dose deposited occurs at the tumour site. One drawback to photons is that they are highly interactive, so dose is deposited all along the beam's path both before and after the tumour.

Electron beams are produced in the same way as photon beams except the target is removed. A cutout is used to shape the beam. Electrons have a finite range, so they are typically used for skin cancers or shallow tumours.[8] This finite range provides an advantage over photons in that deeper structures beyond the tumour are spared from receiving dose.[8]

A more recent development in EBRT is the use of proton therapy. Proton therapy is a relatively new technology and Canada is the only G8 country that currently does not have any proton therapy centres in use or under construction.[9] Protons are roughly 1800 times heavier than electrons making them much less reactive along the path they travel compared to either photons or electrons. This lack of reactivity means that less dose is distributed to healthy tissue that the

protons pass through before reaching the tumour.[9] A large majority of the energy is deposited when the proton reaches the end of its range. The proton beams are adjusted so that the end of their range is the location of the tumour.[9] In 2014 Alberta Health Services created guidelines recommending proton therapy for base-of-skull tumours, most pediatric cancers, intraocular cancers and some central nervous system tumours in adults.[9] One disadvantage to proton therapy is the amount of space required for the unit and supporting equipment compared to a photon therapy unit. One report found a typical photon therapy unit covered a footprint of $75m^2$ on a single storey whereas a proton therapy unit required three stories covering between $111m^2$ to $2000m^2$.[9]

1.3.2 Treatment Planning

Treatment planning for EBRT is typically a combination effort between the radiation oncologist (RO), radiation therapist, dosimetrist, and medical physicist. Once cancer has been detected and EBRT is chosen as a method of treatment, a patient will go through what is known as a simulation. This involves the patient lying on a bed in the position they would be in for their treatment. Small permanent marks are made on the patient's skin to identify where the radiation should be focused. The patient is then imaged around this area typically using CT. The RO will view these images and contour the tumour. This is known as the gross tumour volume (GTV). The GTV represents the physical tumour that is visible.[10] Cancer isn't contained to just the visible tumour; through experience and training the radiation oncologist will also define a clinical target volume (CTV). This CTV is representative of potential microscopic spread of the cancer cells including into lymph nodes.[10] Depending on the location of the tumour an internal target volume (ITV) may be defined. This ITV will take into account motion or compression of the tumour caused by things such as breathing, heart beat or swallowing.[10] The size of the ITV will depend on the amount of motion or compression and is unlikely to be symmetric around the CTV.[10] Finally in order to account for set up errors, machine reproducibility and other human factors, a further margin called the planned treatment volume (PTV) is included.[10] Figure 1.1 shows a visual representation of the volumes used in treatment planning. The margins introduced by the ITV and PTV combined are on the order of a few millimeters. The RO will prescribe a dose typically in Greys (Gy) that the treatment volume or a large portion (90-95%) of the treatment volume should receive. Depending on multiple factors this dose could be delivered in a single fraction on one day or with multiple fractions given over several weeks.

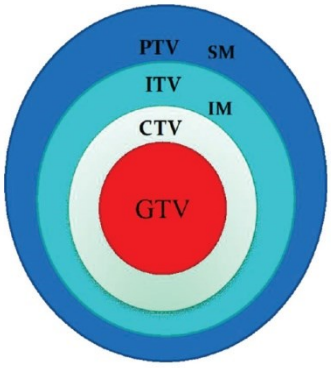

Figure 1.1: A visual representation of the various treatment volumes which would be defined by the radiation oncologist.[11] IM and SM are the internal margin and set up margin respectively used to define the Internal target volume (ITV) and Planned treatment volume (PTV).

The RO will also define and contour organs at risk near the tumour. These are organs that will be in the path of the radiation beam and will receive radiation. The RO will define an acceptable dose that they are willing to tolerate for these organs. The dosimetrists and medical physicists will take this information and design a treatment plan. This treatment plan will define the beam angles used and the intensity of each beam. This treatment plan will then get signed off by the medical physicist and RO and the patient can begin treatment. Several factors, such as dramatic weight loss by the patient and significant shrinkage of the tumour could lead to a re-planning part way through the treatment as the anatomy of the patient will have changed significantly which could change where the radiation is going. Advances in technology such as the integration of MRI, for real-time imaging and tumour tracking during treatment (Linac-MR), could allow for the IM and SM to be reduced which would mean more healthy tissue could be spared.

1.4 MRI

Magnetic Resonance Imaging (MRI) is an imaging modality involving the use of magnetic fields to attain frequency data of the body in order to ultimately create an image.

1.4.1 Hardware

The main hardware for a MR system is broken up into three components: the main magnet, the gradient coils and the RF coils. Figure 1.2 shows the location of each of these components within a typical scanner.

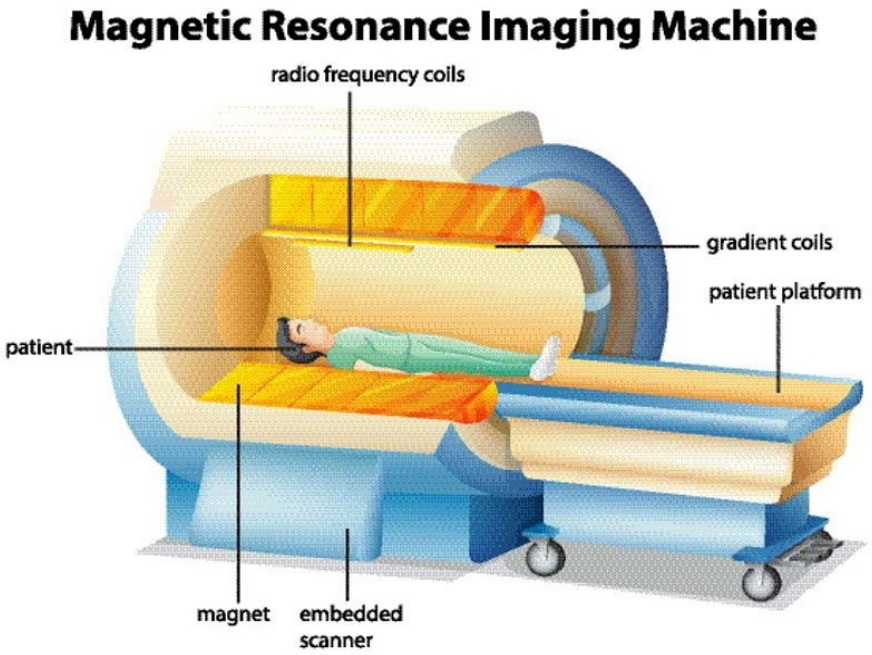

Figure 1.2: The location of each of the components within the MR scanner Image from BlueRingMedia/Shutterstock.com.

Many MR scanners are closed bore systems. The B_o field is created by passing a current through thousands of tightly wound coils in the body of the scanner. This follows with Ampere's Law in a solenoid where:

$$B_o = \mu n I \qquad (1.1)$$

where μ is the permeability of free space, n is the number of turns N divided by the unit length L, and I is the current in Amperes.

Conventionally these coils are kept at very low temperatures using liquid helium in order to maintain super conductivity.

The gradient coils are loops of wire or foil within the bore of the magnet. When current is passed through these wires a secondary magnetic field is created which adds to the primary magnetic field creating deviations in frequency based on position. Gradient fields can be applied in the x, y and z directions. They can also be combined in such a way that a gradient field can be applied in any arbitrary direction. Each of these gradients is powered by an independent power amplifier.

The RF coils on a MR system serve two purposes. First is to transmit RF signals such as the B_1 field and second is to receive the RF signals from the body to produce the frequency data needed to create an image. Coils can be transmit only, receive only or a combination of both transmit and receive. They can be broken up into volume coils or surface coils. Volume coils are cylindrical coils placed around the anatomy of interest to be imaged.[12] Some examples of volume coils are the birdcage and the transverse electromagnetic resonator.[12] Surface coils are partial loops of wire placed on the surface of the patient and are typically grouped together in arrays the size of the area of interest to be imaged. The coils are designed so that they resonate at the same frequency as the protons in the body.[12] Several surface coils placed together are known as an array. Due to the inhomogeneous RF fields produced by the coils, surface coils are typically receive only coils.[12]

1.4.2 MRI Mechanics

Atoms in the body contain magnetic spin properties. When an atom, such as hydrogen, has unpaired protons or neutrons and is subject to a large magnetic field such as the one produced by the main magnet of a MR scanner, it will align with the axis parallel to the direction of the magnetic field or 180 degrees from the direction of the magnetic field, due to the atom's magnetic moments, causing a net magnetization in the direction of the magnetic field. Typical clinical magnet strengths are 1.5T and 3T and are referred to as the B_o field. An RF pulse, known as the B_1 field, is applied perpendicular to the B_o field. This B_1 pulse will tip the net magnetization into the x-y plane causing the magnetization to de-phase and precess at a frequency known as the Larmor frequency. The amount the magnetization is flipped into the x-y plane is known as the flip angle which is controlled by the strength of the RF pulse.

The Larmor frequency is the frequency at which the magnetization precesses. It is dependent on the atom that is precessing and the strength of the B_o field such that:[13]

$$f_o = \gamma B_o \quad (1.2)$$

where f_o is the Larmor frequency and γ is the gyromagnetic ratio which is unique to each nucleus.

Every coil and RF pulse must be tuned to the Larmor frequency.[13] The part of the magnetization in the x-y plane is what provides the signal which is received by the coils. Over time the

polarization will revert to the original magnetization in the z axis aligned with the B_o field, this is known as relaxation. Relaxation times are dependent on the material and the strength of the B_o field. The relaxation time for the magnetization to return to the original B_o direction is referred to as T_1 relaxation. The time it takes for the x-y component of the magnetization to decay is referred to as T_2 relaxation. T_1 and T_2 do not equal each other. Because of inhomogeneites and other imperfections in the scanner a third relaxation time known as T_2* is also used to characterize magnetization relaxation.

Gradient fields are used to control the volume of excitation in the area of the body that is of interest for imaging and provide positioning information using frequency data. When a gradient field is applied it causes a slight frequency shift based off the position of each region of interest. This spatial frequency data is then received by the receiver RF coil. The gradient strengths are changed so that all of the spatial frequency and phase data needed for the scan is acquired. This data is acquired in what is known as k-space. K-space is a Cartesian plot of the spatial frequency data. The central k-space data provides the bulk of the information needed to create an image while the outer k-space data increases sharpness and detail within the image. Each data point within k-space does not correspond to the same pixel within the final image; instead, each point in k-space provides a certain amount of frequency information to each pixel in the final image. In order to go from k-space to the final image a Fourier transform is performed.

1.4.3 Modality comparison

MRI as an imaging modality comes with advantages and disadvantages when compared to other imaging modalities such as CT or ultrasound. Unlike CT and X-Ray, MRI does not rely on ionizing radiation to perform imaging. Instead, it utilizes strong magnetic fields and rf signals, which are safer to tissue than the ionizing radiation. MRI provides superior soft tissue detail compared to CT and X-Ray. X-Ray is limited to 2D superimposed images whereas CT and MRI can provide 3D coverage. Higher spatial resolution is easier to achieve with a CT scan, however MRI is preferred in cases where contrast resolution is required as in regions of soft tissue.

Ultrasound is another modality that does not use ionizing radiation; instead, it uses high frequency sound waves. Compared to MRI, it can provide higher resolution images for structures that aren't particularly deep in the body and can show images in real-time almost as if you were watching a movie.[14] This resolution drops off significantly when the structure of interest is deep

in the body making MRI the preferred choice in these cases. Ultrasound does not require a patient to lie in a bore which is advantageous for patients who may be too large for a MR scanner bore.[14] Ultrasound is limited in the size of area that can be imaged at one time. If the area of interest is too large an MRI would be needed instead. Ultrasound is also limited in its penetration power within structures of the body, which is not a limitation of MRI, so MRI is preferred when the region of interest is within a structure such as a joint that has many different material properties.

Due to the use of strong magnetic fields, MRI is not a suitable imaging modality for people with metal or electronic implants which are not deemed MRI safe or for people who have the potential for unremoved ferromagnetic shrapnel or metal fragments in or around their eyes due to working with metal, accidents earlier in life or other reasons.[15] MRI is a more costly system to build and run when compared to other methods such as CT and ultrasound.[15] MRI is also a potentially slower imaging modality due to the sequence being used. Typical scan sessions, including setup and the scanning itself, run between 30-60 minutes compared to 15-20 minutes for CT and X-Ray.[15] These slow scan sessions can potentially lead to claustrophobia to patients while they lie in the bore of the magnet.

1.5 Linac-MR

1.5.1 Background

In recent years progress has been made in the development and implementation of hybrid Linac-MR systems. These systems combine the magnet of an MRI system with the linear accelerator (Linac) used in radiation therapy. The goal of the Linac-MR system is to be able to provide real-time imaging during a radiation therapy session. Real-time imaging will provide an accurate picture of the tumour location and its movement over the course of a treatment. During standard treatment the location of the tumour is estimated based off pre-treatment imaging. This requires the addition of treatment margins, as discussed above, to the treatment plan. The addition of real-time imaging to radiation therapy can allow for these margins to be reduced, thus sparing healthy tissue in the process.

A few groups around the world are designing their own version of a Linac-MR system each with their own unique specifications. One such system is the Elekta Unity. This Linac-MR combines a

1.5T MR Scanner with a linear accelerator with a 7MV flattening filter free (FFF) beam.[16] Another group in Australia is developing their own Linac-MR system. Their system utilizes a 1T open bore MR scanner with a 6MV linac.[17] An open bore model for a MR scanner allows for more space for the patient reducing claustrophobia and allowing larger patients to be scanned. Open bore MR scanners typically have lower magnet strength than closed bore scanners which can potentially lead to reduced signal. ViewRay has developed multiple versions. The first combined a 0.35T MR scanner with three Co-60 heads as a substitute for the linear accelerator.[18] This has been treating patients since 2014. They have more recently developed a Linac-MR system which still utilizes the 0.35T magnet but replaces the three Co-60 heads with a 6FFF linac.[18] This has been treating patients since 2017.

1.5.2 Linac-MR at the Cross Cancer Institute

At the Cross Cancer Institute (CCI) a group led by the Dr. Gino Fallone has been developing their own Linac-MR system. This system was developed in three stages. The first prototype combined a 6MV linac with a 0.2T permanent magnet.[19] In this prototype the magnet position was fixed while the linac was allowed to rotate. This prototype demonstrated that real-time MR imaging is possible while also performing radiation therapy.[19] One of the issues with combining a linac with an MR magnet is the interference they create for each other. As discussed above MR uses radiofrequency signals in order to get position data in order to create an image. The linac also produces its own radiofrequency signals that will interfere with the ones produced by the MR coils. Concurrently the magnetic field generated by the magnet can interfere with the electrons in the wave guide used to produce the photons for the radiation therapy. This prototype demonstrated one effective method of adequately shielding the wave guide and removing radiofrequency interference from the linac. A special in house RF cage was designed and built to be placed around the MR magnet in order to prevent RF interference.[20] The shielding effectiveness for this cage against E and H fields were found to be above 90dB for frequencies between 1-10MHz and above 100dB at frequencies greater than 10MHz.[20] In order to deal with the magnetic field effects on the radiation beam, active and passive shielding methods have been developed.[21] Further to this, testing has been done on the lingering magnetic fields on both the waveguide, due to transverse fields, and on the dose distribution, due to the longitudinal fields,

because of the shielding not being 100% effective.[21-22] At the low magnetic field strengths proposed by our group, the strength of the unshielded magnetic fields is predicted to be between 0.0022 and 0.011T.[22] These field strengths resulted in beam losses between 1 and 16% in terms of peak intensity of the electron distribution at the electron target compared to no magnetic field being present, however this beam loss resulted in minimal losses in the dose distribution.[22] To test the effects of transverse fields on the waveguide, field strengths up to .0014T, where 100% beam loss occurred, were tested. It was found that even at .0014T the change in frequency in the waveguide were well within the manufacture's tolerances.[21] Because of this, it is predicted that there will be no effect on the accelerator efficiency due to magnetic fields.[21]

The second prototype combined a 6MV linac with a commercial superconducting 0.5T open bore magnet.[23] The purpose of this prototype was to demonstrate the structural and mechanical integrity of the system involving a rotating gantry.[23] This prototype allows the gantry to rotate a full 360° which would allow for more complex radiation treatments when implemented clinically.[23] The third prototype is the clinical version of this system. It combines a 6MV linac with a 0.5T superconducting magnet. As with the second prototype, the magnet is kept at superconducting temperatures using a cryocooler which precludes the need for cryogenic liquids such as liquid helium.[23] At the time of this writing the prototype is undergoing MRI and radiation testing in anticipation of clinical use.

1.6 Contouring

1.6.1 Background

In standard EBRT a patient will undergo a planning CT or MR scan where they will lay in the position that they will be treated in and the area to be irradiated is imaged. In both circumstances a radiation oncologist (RO) will view the resulting images and define the tumour region using contours. They will contour this region on every slice that was acquired. The RO draws these contours with the help of computer software. As discussed above the RO will also contour the other treatment volumes needed for treatment planning.

The use of real-time imaging during radiation treatment will allow for tracking of the tumour in order to adjust the radiation beam or turn it off altogether if the tumour moves outside of an accepted range. Real-time imaging will produce many images very quickly, potentially four

frames a second or more. This could be problematic as it would be too many images for an RO to manually contour or it would take too much time to maintain the real-time characteristics of the imaging. Because of this, many groups are developing and implementing automatic tumour tracking systems for use in real-time imaging. Many of these systems involve indirect tracking using surrogate tumours.[24] A group at the CCI has been developing a direct tumour tracking algorithm using neural networks.[24]

1.6.2 Auto-contouring algorithm

The gold standard for contouring is considered to be the manually drawn contours of a physician.[24] The goal of the work at the CCI is to develop an automated process capable of contouring in a way that is as similar as possible to that of a physician.[24] This method utilizes pulse-coupled neural networks (PCNN).[24] PCNNs were initially proposed to emulate mammalian, including human, visual properties, which is ideal if you are trying to mimic the contouring ability of a physician.[24] The algorithm works under the assumption that a pre-treatment imaging session (~30 frames) is performed. These 30 images are manually contoured by a physician and then given to the neural network as training data. The neural network parameters are optimized so that the shape and location of the auto generated contour most closely resembles that of the manually generated contour from the physician.[24] Following parameter optimization the algorithm is ready for use during treatment.

Prior to an autocontouring session, a single tumour contour that is the least impacted by motion artifacts during breathing is selected (often at the end of exhale phase) from pre-treatment images. Also, a background region that represents the maximum anticipated range of tumor motion is delineated. The neural network will make an assumption that the tumour is located in this background region.[24] During autocontouring, cross-correlation technique is applied between the single tumour contour and the Background, in order to find the most probable tumour location within the background. Centered at this tumour location, the PCNN is applied for tumor contrast improvement from its surrounding anatomy. Finally, Otsu's method of pixel thresholding was used to transform the contrast-enhanced tumour region in the grey scale image into a binary tumour contour.[24]

The algorithm described above was used in this work to determine the contourability of the images that were reconstructed using the method described in this thesis.

1.7 Principal Component Analysis

Principal Component Analysis (PCA) is a mathematical operation used on large data sets that allows for a reduction of dimensions while maintaining the most important data. The goal of PCA is to create a new set of variables (principal components) each of which are linearly independent to each other. The number of principal components will be equal to the number of variables in the original dataset (*D*). An example would be having k-space data of size M×N and acquiring this data from J frames. Initially *D* (Figure 1.3) is of size M×N×J, where J is the number of variables. For PCA this needs to be reduced to a two dimensional matrix of size (M*N)×J.

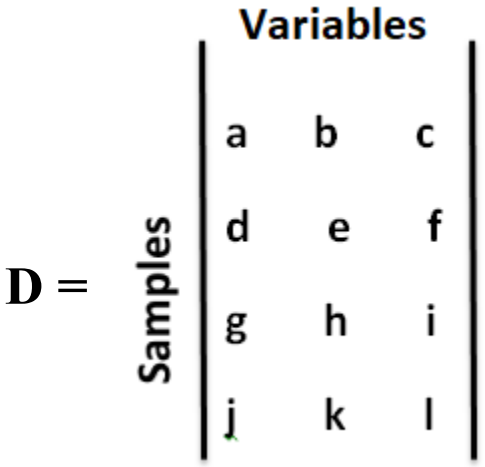

Figure 1.3: The initial data set D. Each column represents a different variable (for example x,y,z). Each row represents a separate sample.

PCA is an eigenvalue/eigenvector problem. Initially a covariance matrix (*COV*) is calculated such that:[25]

$$COV = \frac{1}{J-1} D' \times D. \quad (1.3)$$

D' is the transpose matrix of the initial dataset.

A covariance matrix is a square matrix of size J×J as shown in Figure 1.4 for J=3. The diagonal points represent the variance within each variable. The off-diagonal points represent the covariance (i.e. correlation) between each of the variables.

$$\mathbf{COV} = \begin{bmatrix} \mathrm{Var}(X) & \mathrm{Cov}(X,Y) & \mathrm{Cov}(X,Z) \\ \mathrm{Cov}(X,Y) & \mathrm{Var}(Y) & \mathrm{Cov}(Y,Z) \\ \mathrm{Cov}(X,Z) & \mathrm{Cov}(Y,Z) & \mathrm{Var}(Z) \end{bmatrix}$$

Figure 1.4: An example covariance matrix for J=3.[26] In this example, X, Y and Z are variables represented by the columns of D.

The eigenvalues (*e*) and eigenvectors (*E*) of the covariance matrix are calculated through standard linear algebra techniques i.e.

$$COV * E = eE. \quad (1.4)$$The

Finally, the principal components (*PCs*) can be calculated: [25]

$$PCs = \frac{D * E}{\sum_i e_i}. \quad (1.5)$$

The PCs matrix will be of size J×J. Each column in PCs represents a linearly independent variable. These columns are arranged such that the variable containing the greatest variation is in the first column and each of the subsequent columns is arranged in order of decreasing amount of variation in the variable. Visually each PC can be seen as a line of best fit. Figure 1.5 shows a three-dimensional representation of this. The first PC is the line of best fit through the origin that provides the greatest variation amongst the projections of each data point onto this line. The second PC is then the line of best fit perpendicular to the first PC that provides the greatest variation amongst the projections of the data points. This process is repeated for each principal component making sure that each line of best fit is perpendicular to the other lines.

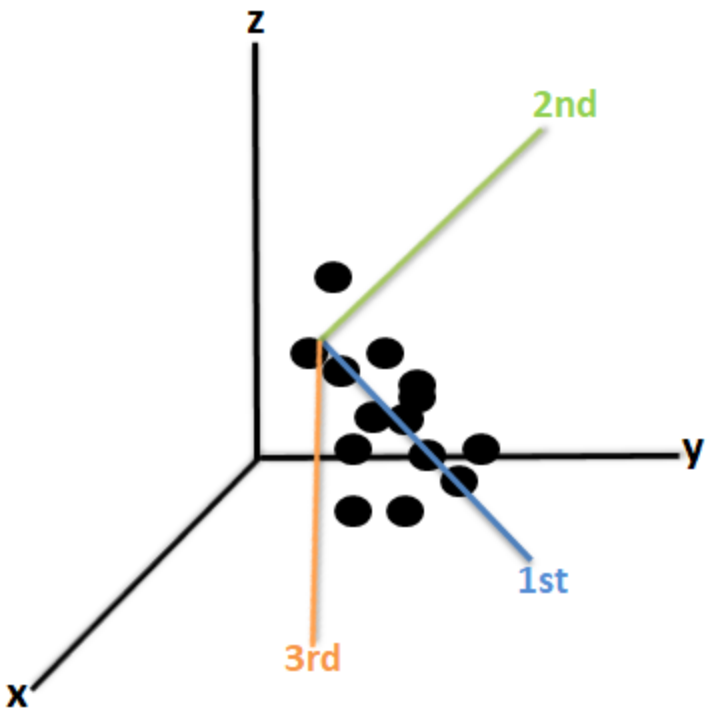

Figure 1.5: A three-dimensional representation of the lines of best fit representing the principal components. The first PC is also considered the largest principal component and contains the greatest variance amongst the original data points.

Since the later columns contain little in terms of variation, they will typically contribute more noise to the data. The dimensionality of the data can be reduced by ignoring the later variables and only keeping the most relevant data so that the final PCs matrix will be of size J×X, where X is a pre-determined number of columns less than or equal to J. A balance needs to be found so that all of the needed information is kept while not introducing too much noise into the system.

PCA is used in a variety of fields with many applications. One example of this is in image compression where an image is resized, and the principal components maintain the most pertinent data. Another example is in finance, where PCA can be used to predict how stocks in a portfolio will behave in the future. In healthcare, PCA is used in a variety of ways. They can be used to correlate disease or outcomes to risk factors. It can also be used on the administrative side for things such as clinical readiness or estimate how long a patient might need to stay at a

hospital. PCA can also be used in patient treatments, as shown with previous work on PCA in MRI along with this work.[25]

1.8 References

1. Canadian Cancer Society, *Canadian Cancer Statistics 2019*, https://cdn.cancer.ca/-/media/files/research/cancer-statistics/2020-statistics/canadian-cancer-statistics/res-cancerstatistics-canadiancancerstatistics-2019-en.pdf?rev=82dc3652fe3648988b9174ad4b397a24&hash=6D3186DF3AC76787C58EE95D1712033C. Accessed April 29, 2021.

2. de Oliveira, C., Weir, S., Rangrej, J., et al. The economic burden of cancer care in Canada: a population-based cost study. *CMAJ Open*, 2018;6(1);E1-E10.

3. Canadian Cancer Society, *Side effects of surgery*, Canadian Cancer Society, https://www.cancer.ca/en/cancer-information/diagnosis-and-treatment/surgery/side-effects-of-surgery/?region=on. Accessed May 3, 2021.

4. Canadian Cancer Society, *Chemotherapy*, Canadian Cancer Society, https://www.cancer.ca/en/cancer-information/diagnosis-and-treatment/chemotherapy-and-other-drug-therapies/chemotherapy/?region=on. Accessed May 3, 2021.

5. Canadian Cancer Society, *Internal radiation therapy*, Canadian Cancer Society, https://www.cancer.ca/en/cancer-information/diagnosis-and-treatment/radiation-therapy/internal-radiation-therapy/?region=on. Accessed May 3, 2021.

6. Canadian Cancer Society, *External radiation therapy,* Canadian Cancer Society, https://www.cancer.ca/en/cancer-information/diagnosis-and-treatment/radiation-therapy/external-radiation-therapy/?region=on. Accessed May 3, 2021.

7. Department of Energy, *How a Particle Accelerator Works*, https://www.energy.gov/articles/how-particle-accelerators-work. Accessed May 3, 2021.

8. University Hospitals Plymouth, *Electron Beam Radiotherapy*, NHS, https://www.plymouthhospitals.nhs.uk/electron-beam-

radiotherapy#:~:text=Electron%20beam%20radiotherapy%20is%20treatment,a%20large%20x%2Dray%20machine. Accessed May 3, 2021.

9. Tsang, D. S., Patel, S. Proton beam therapy for cancer. *CMAJ*, 2019;191(24):E664-E666.

10. Berthelsen, A. K., Dobbs, J., Kjellén, E., et al. What's new in target volume definition for radiologists in ICRU Report 71? How can the ICRU volume definitions be integrated in clinical practice? *Cancer Imaging*, 2007;7(1):104-116.

11. Journal of Medical Physics, *Figure 1: The internal target volume defined by ICRU 62*, https://www.jmp.org.in/viewimage.asp?img=JMedPhys_2017_42_3_101_214491_f1.jpg. May 5, 2021.

12. Gruber, B., Froeling, M., Leiner, T., Klomp , D. W. RF Coils: A Practical Guide for Nonphysicists. *Journal of Magnetic Resonance Imaging*, 2018;48:590-604.

13. Elster, A. D. (2021). *Larmor Frequency*. (ELSTER LLC) http://mriquestions.com/why-at-larmor-frequency.html. Accessed May 6, 2021.

14. Cleveland Clinic, *When Is Ultrasound Used vs. an MRI for Bone, Muscle and Joint Problems?*, https://health.clevelandclinic.org/when-is-ultrasound-used-vs-an-mri-for-bone-muscle-and-joint-problems/. Accessed June 21, 2021.

15. Davis, C. P. *CT Scan vs. MRI Differences between Machines, Costs, Uses.* (MedicineNet) https://www.medicinenet.com/ct_scan_vs_mri/article.html. Accessed June 22, 2021.

16. Elekta, *Elekta Unity: Two worlds one future*, https://www.elekta.com/dam/jcr:3883d2d4-d9e7-449d-84e2-815532681287/Elekta-Unity-Brochure.pdf. Accessed June 25, 2021.

17. Keall, P. J., Barton, M., Crozier, S. The Australian magnetic resonance imaging-linac program. *Radiother Oncol,* 2014;18:203-206.

18. Klüter, S. Technical design and concept of a 0.35 T MR-Linac. *Clinical and Translational Radiation Oncology*, 2019;18:98-101.

19. Fallone, B.G., Murray, B., Rathee, S., et al. First MR images obtained during megavoltage photon irradiation from a prototype integrated linac-MR system. *Medical Physics*, 2009;36(6):2084-2088. doi:10.1118/1.3125662

20. Lamey, M., Burke, B., Blosser, E., Rathee, S., De Zanche, N., Fallone, B. G. Radio frequency shielding for a linac-MRI system. *Physics in Medicine and Biology*, 2010;55:995-1006.

21. St. Aubin, J., Steciw, S., Fallone, B. G. Waveguide detuning caused by transverse magnetic fields on a simulated in-line 6 MV linac. *Medical Physics*, 2010;37(9):4751-4754.

22. St. Aubin, J., Santos, D. M., Steciw, S., Fallone, B. G. Effect of longitudinal magnetic fields on a simulated in-line 6 MV linac. Medical Physics, 2010;37(9):4916-4923.

23. Fallone, B. G. The Rotating Biplanar Linac–Magnetic Resonance Imaging System. *Seminars in Radiation Oncology*, 2014;24:200-202.

24. Yun, J., Yip, E., Gabos, Z., Wachowicz, K., Rathee, S., Fallone, B. G. Neural-network based autocontouring algorithm for intrafractional lung-tumor tracking using Linac-MR. *Med Phys*, 2015;42(5):2296-2310.

25. Dietz, B., Yip, E., Yun, J., Fallone, B. G., Wachowicz, K. Real-time dynamic MR image reconstruction using compressed sensing and principal component analysis (CS-PCA): Demonstration in lung tumor tracking. *Medical Physics*, 2017;44(8):3978-3989.

26. StackExchange. *Making sense of principal component analysis, eigenvectors & eigenvalues*. https://stats.stackexchange.com/questions/2691/making-sense-of-principal-component-analysis-eigenvectors-eigenvalues. Accessed August 19, 2021.

Chapter 2

Time Domain PCA MR Algorithm

A version of this chapter has been published as: Wright M, Dietz B, Yip E, Yun J, Gabos Z, Fallone BG, Wachowicz K. Time Domain Principal Component Analysis for Rapid, Real-Time 2D MRI Reconstruction from Undersampled Data. *Medical Physics*. 2021;48:6724-6739. https://doi.org/10.1002/mp.15238

2.1 Introduction

The integration of real-time MR imaging with radiotherapy can allow for on-the-fly beam adjustments to accommodate mobile patient anatomy. One of the fundamental benefits behind this type of real-time adaptive radiotherapy is the ability to reduce treatment margins and spare healthy tissue while focusing more precisely on the tumor. Several groups have developed hybrid linac-MR machines in order to achieve adaptive radiotherapy in real time.[1-4] However, the majority of MR scanning techniques are not practical for real-time dynamic imaging, which can take several minutes for a single acquisition. Lengthy scan times pose a problem for real-time imaging, where speed is important in order to maintain an accurate representation of the current state of the anatomy. While some conventional sequences exist that produce sufficient frame rate for real-time purposes (such as balanced steady-state free precession, or bSSFP), conventional implementations are generally limited to low-resolution 2D coverage.[5-7] The use of acceleration techniques expands possibilities for frame rate, resolution, and multi-slice coverage for sequences like bSSFP, and could allow for other sequences and their different contrasts to be incorporated into the real-time environment. One common strategy in MRI for reducing acquisition time is k-space under-sampling, which comes in many forms, such as parallel imaging, compressed sensing, and neural network reconstructions.[8-10] However, effective parallel imaging solutions require optimized receive coil geometries, which may be limited for some MR systems. Compressed sensing or neural network reconstructions require computationally expensive algorithms that can be a challenge in a real-time guided radiotherapy regime. The

strategy presented in this work uses Principal Component Analysis (PCA) to reconstruct under-sampled data in a temporally robust and computationally inexpensive way.

PCA is a data analysis technique where principal components (PCs) of a data set are computed and used to perform a change of basis on the data. PCA is frequently applied to large data sets and allows for the reduction of data into a more manageable size while maintaining the most significant information. The PCs are directional vectors that are representative of the primary modes of variation within the data set. These components are calculated by finding an orthogonal basis set which orders the dimensions from greatest to least amount of variation. The dimensions with the least amount of variation can be attributed mostly to noise and removed.

Previous work by Dietz et al. investigated using PCA to establish PCs of variation that correspond to the spatial domain; components that were then sparsely fitted frame-by-frame to subsequent undersampled data for on-the-fly MRI reconstruction.[11] In that method, PCA was implemented on a database of fully-sampled images taken immediately prior to accelerated reconstruction. While that technique produced images suitable for real-time tracking, it was observed that the accelerated image quality worsened as time increased from when the database was acquired. The goal of this current work is to generate a new PCA-based algorithm to create a more time-robust method of real-time reconstruction from undersampled data.

In our proposed method, the calculated PCs will be representative of the time evolution of k-space (rather than variation within image frames) and will be continuously updated. We believe this temporal approach will allow for a more robust MR acceleration and lead to a more consistent image quality over time. Previous studies have utilized time-domain PCA for MRI. Most of these studies have focused on rapid fMRI or as an aid for reconstruction in large k-space-time (k-t) undersampled data sets.[12-14] Our technique was designed specifically to work on-the-fly and reconstruct images with minimal latency, using PCA to predict and fill undersampled k-space data. The method proposed by Wang et al., for use in fMRI, requires the entire spatial-temporal volume be acquired in advance and reconstructed together using an iterative process.[12] It utilizes PCA in the time domain to improve sparsity for better reconstruction and error suppression.[12] While this method worked very well, it wouldn't be appropriate for our real-time application To our knowledge this is the first implementation of time-domain PCA in an algorithm suitable for real-time 2D low latency applications.

2.2 Materials and Methods

2.2.1 Data acquisition and retrospective undersampling

Fifteen fully-sampled dynamic data sets from subjects with non-small cell lung cancer, acquired with approval from our local ethics committee, were used to test our acceleration method through retrospective analysis. A subset of six of the fifteen patients was used to test the auto-contouring capabilities of this method using neural-network contouring software developed by our group.[15] These patients were imaged using a 3T Philips Achieva Scanner (Phillips Medical Systems, Cleveland, OH, USA) for three or five minutes of free breathing in order to acquire 650 or 1100 dynamic frames. A 2D bSSFP sequence was used for all acquisitions (FOV: 40 x 40 cm^2, pixel size: 3.1 x 3.1 x 20 mm^3, TR/TE = 2.2/1.1 ms, acquisition time for each frame = 275ms, acquisition matrix 128x128x650 or 128x128x1100). The undersampling pattern masks were applied retrospectively to these data sets, to simulate the acquisition of faster framerates.

The data sets are retrospectively undersampled by applying a mask to the fully-sampled data. For a given frame, k-space is sampled differently in two zones. The central k-space (low frequency) data are fully-sampled as a block of phase encodes. These phase encodes are known as the core phase encodes. The size of this core is pre-determined before data acquisition takes place. The outer k-space (high frequency) data is incoherently undersampled. Within each frame the phase encodes are undersampled in adjacent pairs to minimize eddy current artifacts.[16] The undersampling pattern is a part of a set of complementary patterns that are applied over a range of frames. These complementary patterns ensure that all of k-space is acquired within a given number of frames (N_{COMP}). N_{COMP} is dependent on the size of the core and the acceleration rate. The core set of phase encodes are acquired in every frame. These complementary patterns are repeated throughout the scan, and by design fit evenly into a pre-determined number of frames (N_{WIN}) that make up the reconstruction window. The reconstruction window consists of the current frame being reconstructed, and data from the previous (N_{WIN}-1) frames that allow the missing data in the current frame to be predicted. Figure 2.1 provides a visual representation of how the data within a given frame as well as in the entire reconstruction window are retrospectively undersampled. When that frame has been reconstructed the reconstruction window shifts so that next frame can be reconstructed. Figure 2.2 provides a visual representation of our proposed method's workflow. The acceleration rate that is achieved will

depend on the size of the core and N_{COMP}. As such, a particular acceleration rate can be achieved with a variety of different choices. Table 2.1 displays the values that were chosen for the acceleration rates investigated in this work, based on an optimization described below.

Table 2.1: Number of frames to acquire all of k-space and core size used to achieve a particular acceleration rate, assuming 128 phase encodes in a fully-sampled data set. In this case, Acceleration Rate = 128 / (Core Size + (128-Core Size)/N_{COMP}) where N_{COMP} is the number of frames forming a complementary set. Values of N_{COMP} and Core size were selected for a particular acceleration rate by optimizing image quality metrics.

Acceleration Rate	N_{COMP}	Core size
3	4	16
4	5	8
5	10	14
6	10	10
8	15	8

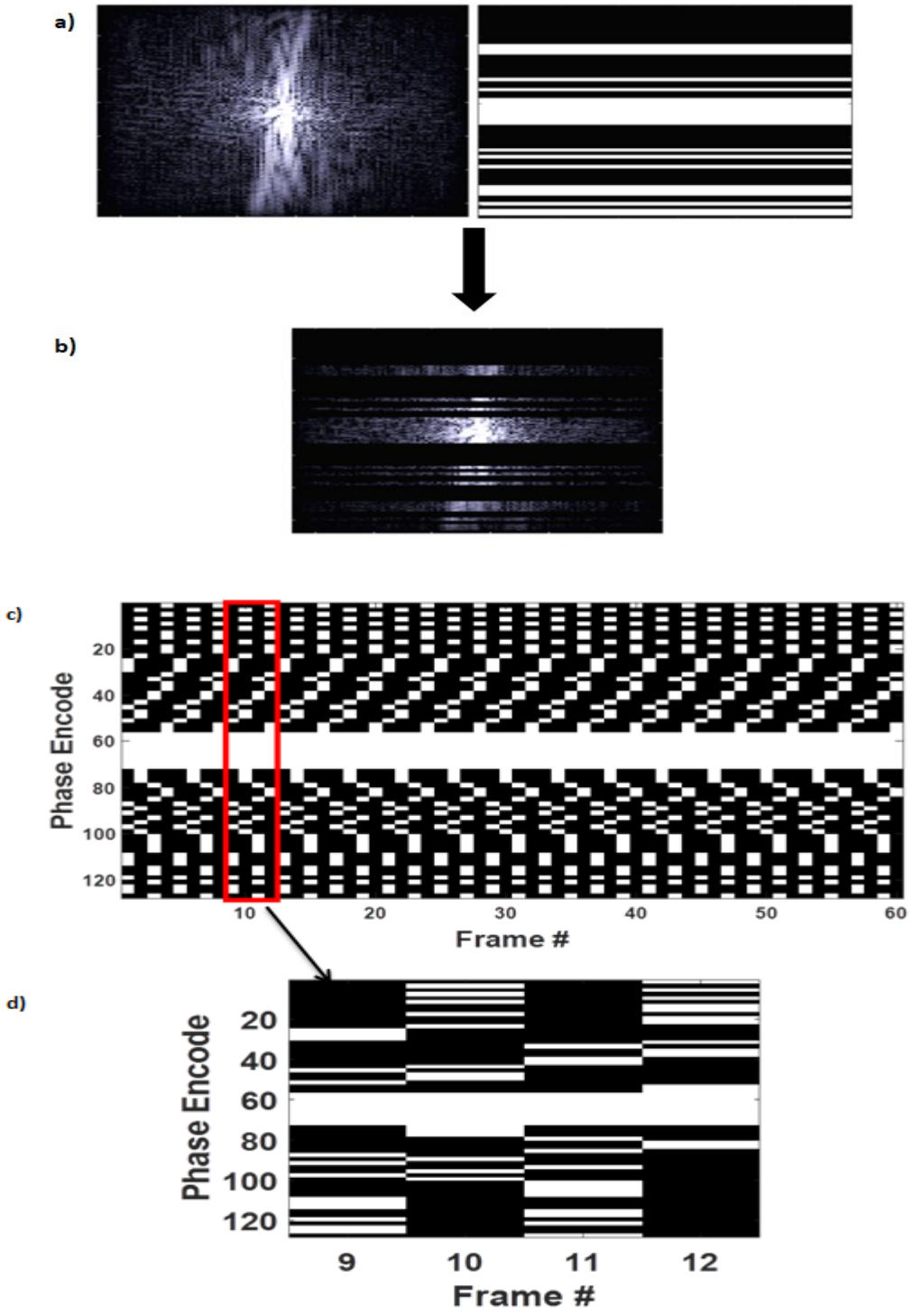

Figure 2.1: A visual representation of how the data is retrospectively undersampled. a) A mask representing an incoherent undersampling pattern is applied to the full- sampled k-space data, creating a simulated undersampled k-space b). Note that the mask is comprised of randomly distributed pairs of adjacent phase encodes along with a non-random set of core PEs. c) represents how the masks are cycled within the reconstruction window of sixty frames. Highlighted is a single complementary set representing an N_{COMP} value of 4. This highlighted zone could be placed at any arbitrary point within the window and still encapsulate a complementary set. d) is an expanded version of this window

2.2.2 Principal component development and image reconstruction

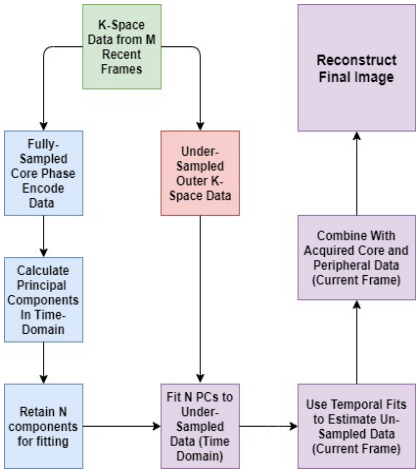

Figure 2.2: Flow chart of the acceleration method. All calculations are done in the k-space domain. The initial green square represents the raw data, for the M most recent frames. The blue column on the left represents the workflow to generate PCs from core data. The red square represents undersampled outer k-space data. Purple: Through fitting, the blue and the red are combined to generate a fully-sampled version of k-space and finally an image.

Within an undersampling pattern, a pre-determined number of phase encodes at the centre of k-space are acquired for every frame. These core phase encodes are used to calculate the PCs representative of time evolution within a reconstruction window. The original fully-sampled images were acquired using a six coil array and combined. For this retrospective analysis, the combined complex core data is submitted to the MatLab PCA function without any demeaning.[17] Both the real and imaginary portions of the complex data are handled together. Figure 2.3 demonstrates how these principal components are further used to reconstruct the frame of interest. When the window is shifted to reconstruct a new frame, the principal components are recalculated and updated using the data from the new frame while discarding the information from the old frame. This allows us to have the PCs be representative of the most up-to-date information. For our implementation a reconstruction window of 60 frames (arbitrarily chosen) was used for all acceleration rates. Within this window, the last frame will be the one that is reconstructed, for example in the window of frames 1-60; frame 60 will be fully reconstructed. This process is repeated with the window continually shifting for the next frame to be reconstructed (i.e. frames 2-61 to reconstruct frame 61). All data was processed using commercially available software (MATLAB R2019a, The MathWorks Inc., Natick MA, USA) [17]

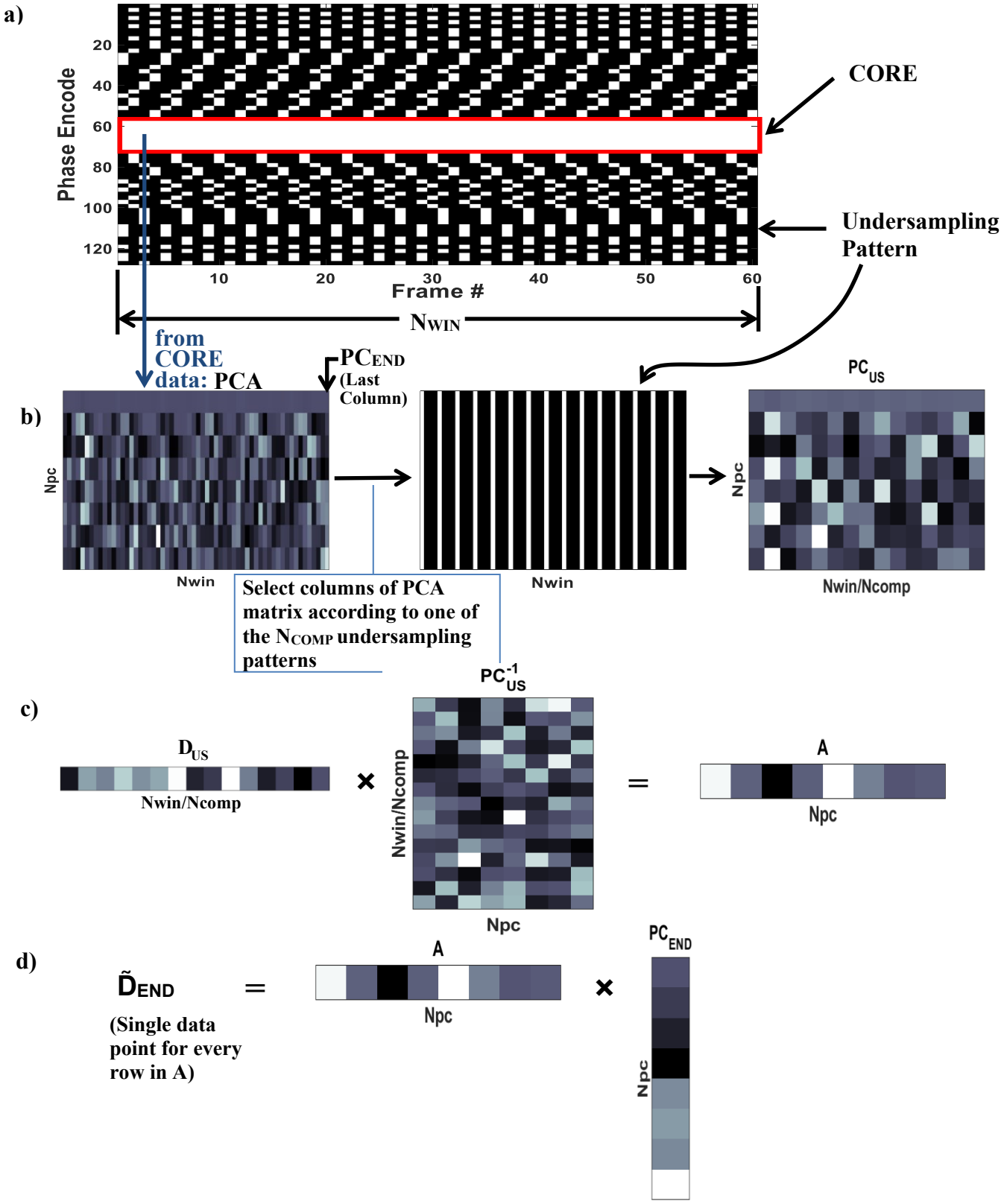

Figure 2.3 a): A representation of the reconstruction window and how the phase encodes are undersampled per

frame. Highlighted (red box) is the core set of phase encodes which are acquired in every frame. Also highlighted (Undersampling Pattern) are the frames containing the same undersampling pattern as the first frame of the reconstruction window. The PCA matrix is undersampled so that only these frames are represented in PC_{US} b) Represents the process of calculating the PCA matrix on the core phase encodes, and undersampling them (PC_{US}) for use in the workflow (only one sampling pattern is shown for demonstration). Each row in the PCA matrix represents a principal component. This process is repeated for each undersampling pattern, except the one that samples data in the final frame of the window. c) The PC_{US} matrix is inverted and multiplied with the undersampled outer k-space data in D_{US} to calculate the amplitudes (A) of the PCs. For demonstration purposes only a single row of D_{US} and A are shown. d) The final step involves combining the amplitudes, A with the PC data calculated from the core data corresponding to the frame being reconstructed, PC_{END}. This provides an estimate for the missing k-space data giving $\widetilde{D}_{END}$

A pre-determined number of the already calculated PCs (N_{PC}) are fitted to the undersampled data within the time domain by using the Moore-Penrose pseudoinverse matrix, a generalization of the inverse matrix.[18] This generalized matrix can be used to invert non-square matrices which are required for our proposed application. This fitting method allows for the un-acquired data in the frame of interest to be filled in using a multi-step process. The following equations represent the work flow of the algorithm and are illustrated graphically in Figure 2.3. The undersampled data, D_{US}, can be estimated by a linear combination of the undersampled Principal Components (PC_{US}) with amplitudes, A.

$$D_{US} \cong A * PC_{US}. \qquad (2.1)$$

PC_{US} is a matrix of the size $N_{PC} \times (N_{WIN}/N_{COMP})$. D_{US} represents the undersampled k-space data outside of the core corresponding to one of the unique undersampling patterns. It is represented by one row in Figure 2.3 for demonstration, but in practice it will contain ($N_{RE} \times (N_{PE} - Core)/N_{COMP}$) rows, one for each point in k-space sampled with this pattern, and N_{WIN}/N_{COMP} columns. N_{RE} and N_{PE} represent the number of read and phase encodes respectively, and Core is the number of phase encodes in the core. Since this has already been acquired and the undersampled PCs (PC_{US}) calculated, it is the amplitudes (A) that need to be calculated:

$$A = D_{US} * PC_{US}^{-1}. \qquad (2.2)$$

The amplitudes represent the best fit of the PCs to the acquired outer k-space data from the previous N_{WIN}-1 frames in the reconstruction window. They are multiplied with the PC data

corresponding to the frame being reconstructed, PC_{END}, which generates an estimate of an unacquired point in k-space, $\widetilde{D}_{END}$:

$$\widetilde{D}_{END} = A * PC_{END} = D_{US} * PC_{US}^{-1} * PC_{end}. \quad (2.3)$$

The entire process is repeated N_{COMP}-1 times as one of the undersampling patterns explicitly acquired data for the current frame of interest. Typical reconstruction times are ~50 ms/frame (Intel® Core i5-2430M CPU @ 2.40GHz, 6GB RAM).

To confirm this method has improved temporal robustness, the same data was also processed using the code developed by Dietz et al. using the parameters discussed in their paper.[11] This method utilizes a database of 30 images acquired immediately before the real-time imaging session. The PCs are calculated from this database. Reconstruction is performed iteratively, a pre-determined number of times. Weights are applied to each PC and those that fall below a certain threshold are discarded. The reconstructed images of each method were split into regions and the average value of each metric within that region was recorded. Due to the nature of each method, i.e. reconstruction window size vs database size, only frames common to both methods are used in calculating comparative metrics to ensure both metrics are being generated with the same source data. Using the metrics discussed below the two methods were compared for overall image quality and robustness over time, in addition to contouring accuracy. Further comparison of these metrics was made with a standard low-resolution acquisition of an equivalent acceleration rate.

2.3 Analysis and Metrics

2.3.1 Optimization of reconstruction parameters

The optimal value of N_{PC} was investigated. To prevent an under-determined inverse problem i.e. not enough equations for the number of variables, the actual value of N_{PC} cannot exceed the number of acquired data points within the reconstruction window. The number of acquired data points, N_{SAMP}, is equal to the number of times the complementary set of frames is repeated within the reconstruction window (N_{WIN}/N_{COMP}).

The acceleration factor is controlled by the size of the core phase encodes as well as N_{COMP} which controls the fraction of phase encodes that are sampled outside of the core. Even valued core sizes between eight and sixteen were used in this investigation. Because the acceleration is controlled by both the core and N_{COMP}, different combinations of these can account for the same acceleration factor. Finding the best combination for a particular acceleration factor was investigated using the two patients who showed the best metrics averaged over the entire range of PCs and the two patients who showed the worst metrics averaged over the entire range of PCs for an acceleration factor of three. Normalised mean squared error (NMSE), peak SNR (PSNR) and structural similarity index (SSIM) were again used to compare the results of these combinations in order to determine the best combination of cycles and core size for a particular acceleration. The combination that produced the best results for a particular acceleration was then further tested on the remaining eleven patients to determine the full capabilities of our method at a particular acceleration.

The use of NMSE, PSNR and SSIM were used to investigate the optimal value of N_{PC} and to compare combinations of core size and N_{COMP} for a particular acceleration factor as these are common metrics used in the field for assessment of general image quality. For this study, acceleration factors of three, four, five, six and eight were tested. To test the effects of N_{PC}, a range of two to ten PCs was tested at acceleration rates of 3x and 4x. A range of two to six PCs was tested for acceleration rates of 5x and 6x and for an acceleration rate of 8x a range of two to four PCs was tested. The above ranges were based on preliminary analysis of three patient data sets where it was seen that the optimum values would be in these bounds. Further optimization was performed on a subset of six of these patient data sets to test our method for auto-contouring purposes.

2.3.2 Normalized mean square error

Normalised Mean Square Error (NMSE) can be used to measure artifact level in image reconstruction. A NMSE of zero represents a complete agreement between images, while a value greater than zero represents deviations between the images typically in the form of artifacts.[11] In our study the reconstructed image was always compared to the fully-sampled image. The NMSE can be calculated by taking the square of the difference between the fully-sampled and reconstructed image and dividing by the square of the fully-sampled image.

$$NMSE = \frac{\sum(I_{full} - I_{recon})^2}{\sum I_{full}^2}. \quad (2.4)$$

The average NMSE over the 591 or 1041 frames was calculated for each patient for a varying number of principal components kept, depending on the number of cycles used. The total patient average was calculated for each number of principal components and a total patient aggregate was calculated for acceleration values ranging from 3 to 8.

2.3.3 Peak SNR

The Peak Signal to Noise Ratio (PSNR) is the ratio between the maximum possible value of a signal or image to the power of the distorting noise that affects the signal or image.[19] It can be calculated by:

$$PSNR = 10log_{10}\left(\frac{Max^2}{MSE}\right). \quad (2.5)$$

where *Max* is the maximum value in the reconstructed image and *MSE* is the mean square error between the fully-sampled and reconstructed images. PSNR was used to quantify how much uncertainty is being added in the reconstruction process.

2.3.4 Structural Similarity Index

Structural similarity index (SSIM) is another metric used to measure image quality that takes into account the luminance, contrast and structure of the entire image.[20] In our study the SSIM was calculated using the built in MATLAB function which uses the following formula:[21]

$$SSIM = \frac{(2\mu_F\mu_{US} + C_1)(2\sigma_{F,US} + C_2)}{(\mu_F^2 + \mu_{US}^2 + C_1)(\sigma_F^2 + \sigma_{US}^2 + C_2)}. \quad (2.6)$$

where μ_F, μ_{US}, σ_F, σ_{US} are the means and standard deviations of the fully-sampled and undersampled data, and $\sigma_{F,US}$ is the cross-covariance of the images. The constants *C1* and *C2* are typically chosen based on the dynamic range (DR) of the images: $C1 = (0.01 * DR)^2$ and $C2 = (0.03 * DR)^2$. An SSIM of 1 indicates that the two images do not deviate, while a SSIM less than

one means there is some deviation between the two images. SSIM provides information on the inter-dependency between pixels in an image which is not shown in NMSE or PSNR which only show absolute differences.

2.3.5 Dice coefficient

The Dice coefficient is a metric used to quantify the common coverage of two regions of interest (ROIs), in this case between an ROI contoured on an accelerated reconstruction and one contoured on the fully-sampled image. This was calculated using the built in MATLAB function which uses the following formula:[22]

$$Dice = 2\frac{ROI_{full} \cap ROI_{US}}{ROI_{full} + ROI_{US}}. \qquad (2.7)$$

The Dice coefficient takes into account the overlap between the two ROIs with respect to the sum of the two ROIs. A value of 1 indicates complete agreement between the two images in terms of overlap of the region of interest whereas a value of 0 indicates no overlap of the region of interest for the two images.

2.3.6 Hausdorff distance

The Hausdorff distance is another metric used to determine the similarity of regions of interest. It is defined as the global maximum of the minimum distance between the edge of one ROI and the edge of a second ROI.[23] This was used to compare how much of a difference there was between the contouring done on the fully-sampled image compared to the undersampled image.

2.3.7 Centroid displacement

Centroid displacement was used along with the Dice coefficient and Hausdorff distance to test the real time tracking capabilities of our method. The centroid displacement is the separation between the centroid of the contour calculated from the fully-sampled images and the contour from the undersampled reconstructions.

2.4 Results

2.4.1 Effects of N_{PC}

One of the parameters that can be adjusted in our proposed method is N_{PC}. This parameter was tested on all fifteen patients at acceleration rates of 3x, 4x, 5x, 6x, and 8x. Figure 2.4 is a demonstration of NMSE, SSIM and PSNR for different N_{PC} at different acceleration rates while Figure 2.5 displays the time evolution of a single patient for N_{PC} values of two, four, seven and ten. The advantage of fitting with a larger bank of PCs is more motion detail. However, high numbers of PCs can lead to instabilities in the solution due to an increase in fitting uncertainty. The optimum number of PCs for fitting was found to be 5, 5, 3, 3 and 2 for acceleration rates of 3x, 4x, 5x, 6x and 8x respectively. These values represent the optimal value from an average of all fifteen patients. Individual patients may have had a different optimal value but the mean optimal values worked well for all patients.

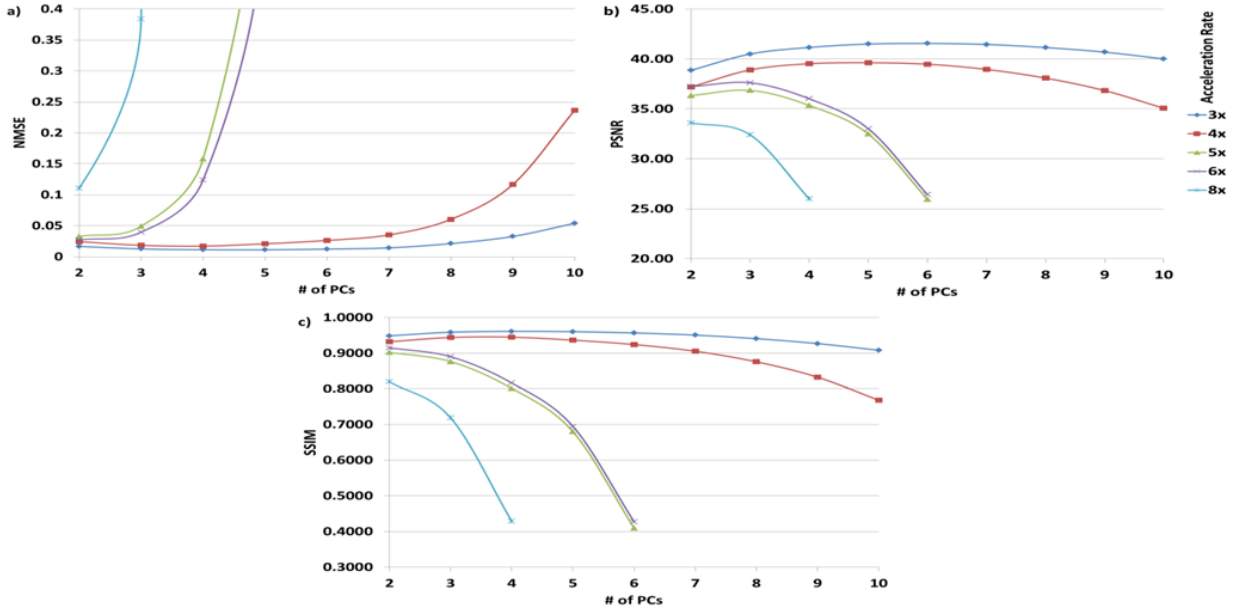

Figure 2.4: Total Patient Average a) NMSE, b) PSNR and c) SSIM as a function of N_{PC} and acceleration rate. Each line represents a different acceleration rate. For a) some of the more poorly performing data points for accelerations greater than 4x are out of frame for purposes of scale

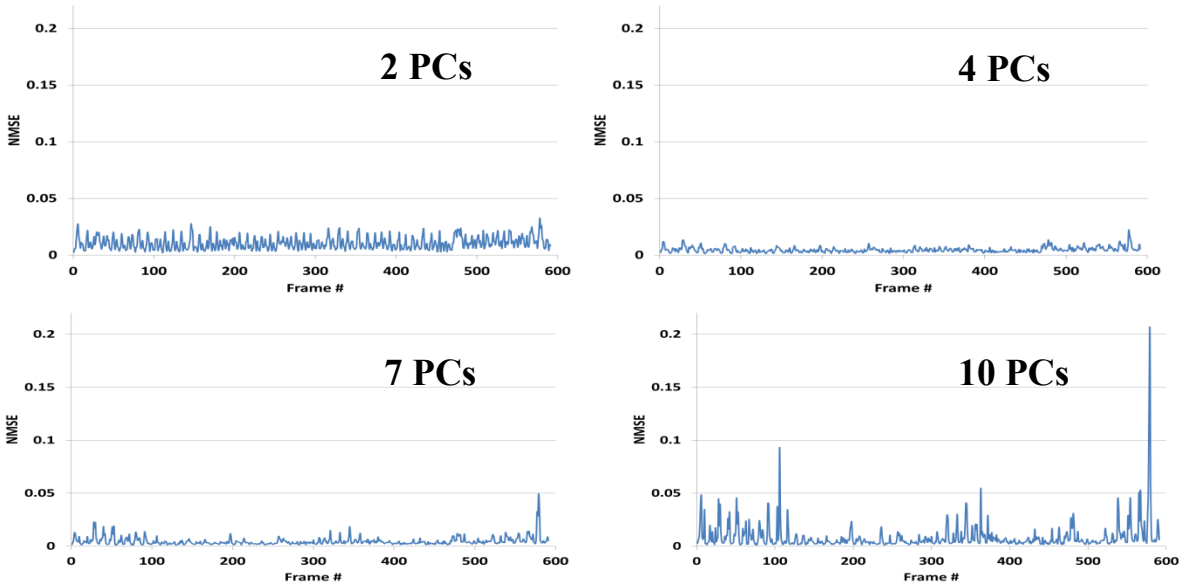

Figure 2.5: Time evolution of NMSE for a single patient for image reconstruction with (clockwise from top left) two, four seven and ten PCs kept. Reconstruction was done at an acceleration rate of 3x.

2.4.2 Temporal robustness

Normalised mean square error (NMSE) was used to track image quality over time. Figure 2.6a and b demonstrate the temporal robustness of the image quality on two patients for the proposed method over the course of a typical treatment time. The figures represent data acquisition at an acceleration factor of 3x with 5 PCs used for reconstruction (found to be optimal for this case). A comparison to the frame-based PCA method proposed by Dietz et al. was included using the same patient data. Figure 2.6c display visual representations of the final acquired frame from the patient data represented in figures 6a and b, comparing the fully-sampled data set (both full k-space and central k-space only acquisitions), our proposed method, and the frame-based PCA method. Also included in Figure 2.6a and b is the breathing pattern of each of the respective patients. Sudden changes in the breathing pattern could potentially lead to degraded image quality. Figure 2.7 demonstrates the temporal robustness of our method over the course of an imaging session while also providing a comparison to the method proposed by Dietz et al.

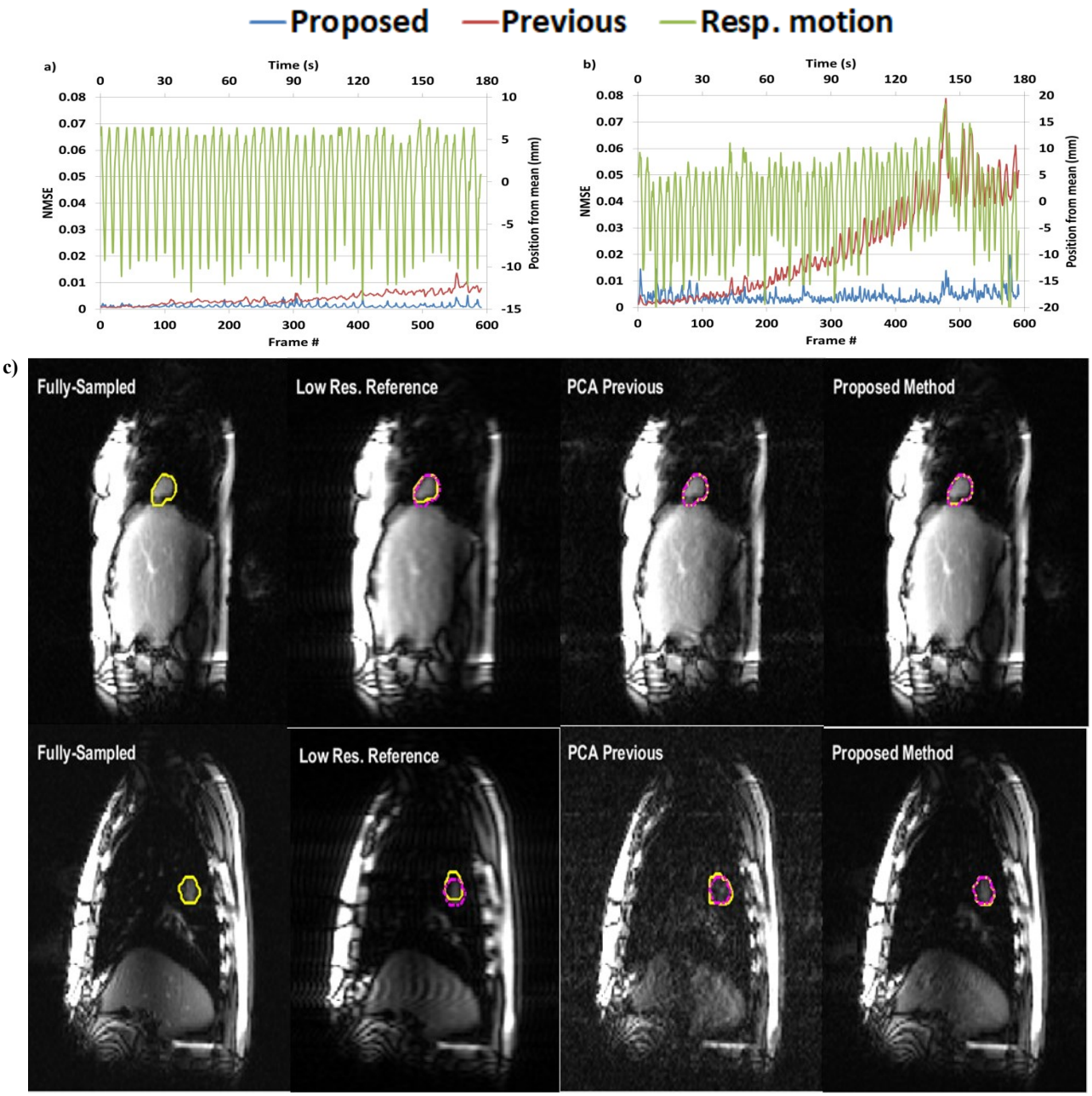

Figure 2.6(a,b): A time evolution comparison of the previous method and our proposed method using Normalised mean square error for two different patient data set using an acceleration factor of 3. Overlaid are respiratory curves representing the relative position of the dome of the diaphragm. (c) is a visual representation of the last frame reconstructed using both methods for the patient represented in a (top) and b (bottom). The fully-sampled reconstruction is included as reference. Also included for reference was a conventional acceleration through 3-fold truncation of k-space, resulting in a lower resolution image. The windowing was set to allow for comparison of noise floor. The contours generated by the auto-contouring software are also included. For the reconstructed images the fully-sampled contour (dashed line) is also included for reference.

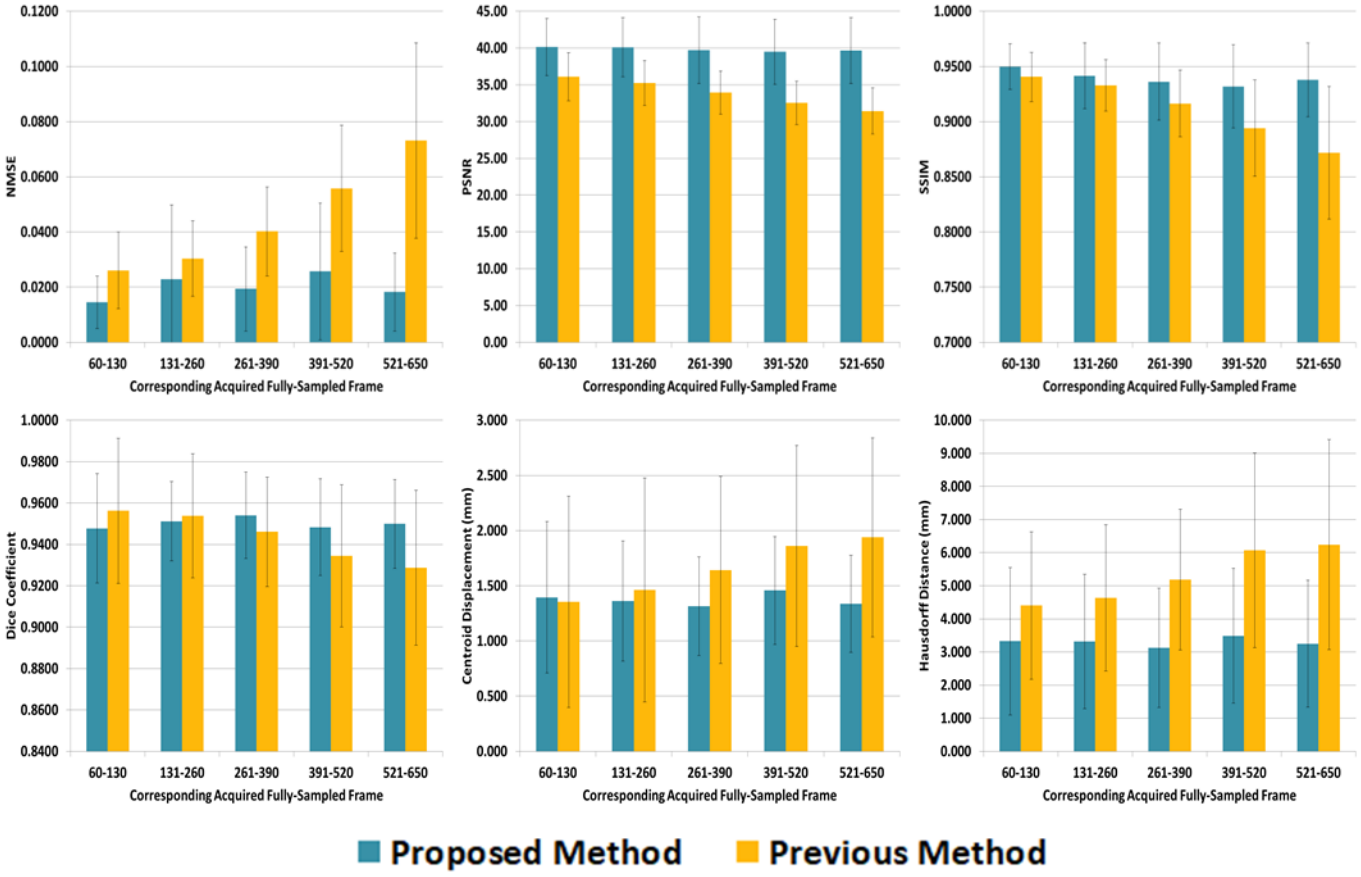

Figure 2.7: A demonstration of the temporal robustness of our method using each of the image quality (NMSE, PSNR and SSIM) and contourability metrics (Dice coefficient, centroid displacement and Hausdorff distance). The reconstructed frames were broken into regions to show the change in metric over time. Each value shown is an average of the 15 patients for the frames of interest. A comparison is also made with the method from Dietz et al. Only common reconstructed frames between the two methods are used for comparison. The frames referenced correspond to the original fully-sampled acquisition.

The impact of increased acceleration rate is shown in Figures 2.8 and 2.9, both as a comparison of the two methods and as a demonstration of the capabilities of our proposed method. The comparison was conducted using the quantitative metrics: NMSE, SSIM and PSNR. The results for our proposed method represent the optimal number of principal components used for fitting which resulted in the best total patient average as shown in Figure 2.4.

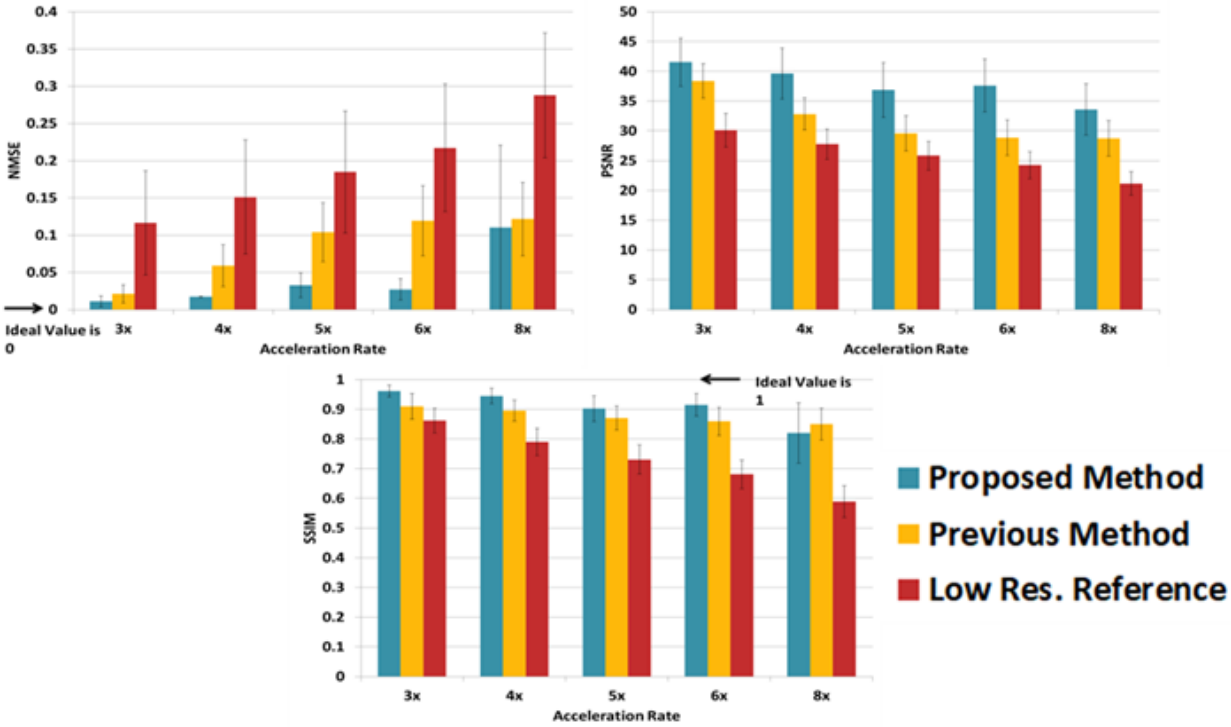

Figure 2.8: Effects of acceleration rate on NMSE a), PSNR b) and SSIM c).Displayed are averages from all patient data sets using the optimal number of PCs for fitting as identified during testing. A comparison was also performed between the previous method proposed by Dietz et al. and our current proposed method. Statistics from a low resolution acquisition equivalent to the same acceleration rate are shown as references.

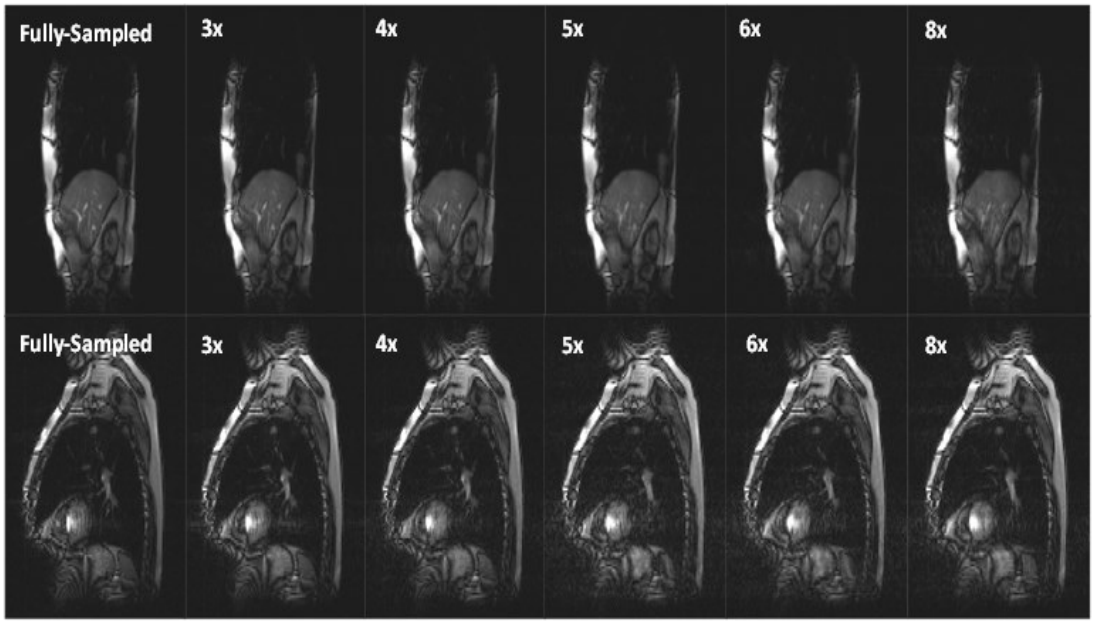

Figure 2.9: A visual representation of the effects of acceleration on the final frame of the best (top) and worst (worst) performing patient data sets. The optimum N_{PC} value for each acceleration was used in the reconstruction. A comparison is also done with the initial fully-sampled image.

2.4.3 Contouring Capabilities

Dice coefficient and Hausdorff distance were used to test the ability of our reconstructed images to contour structures as compared to the same structures identified on the fully-sampled images. Centroid displacement was also tested to measure the accuracy of the region of interest being contoured to the same region of interest on a fully-sampled image. Figure 2.10 shows the impact of acceleration rate on the contour ability and is benchmarked against the previous method by Dietz et al. The results from our method represent the optimal number of principal components fitted to produce the best total patient average. As with the image quality tests, acceleration rates of 3x, 4x, 5x, 6x, and 8x were used.

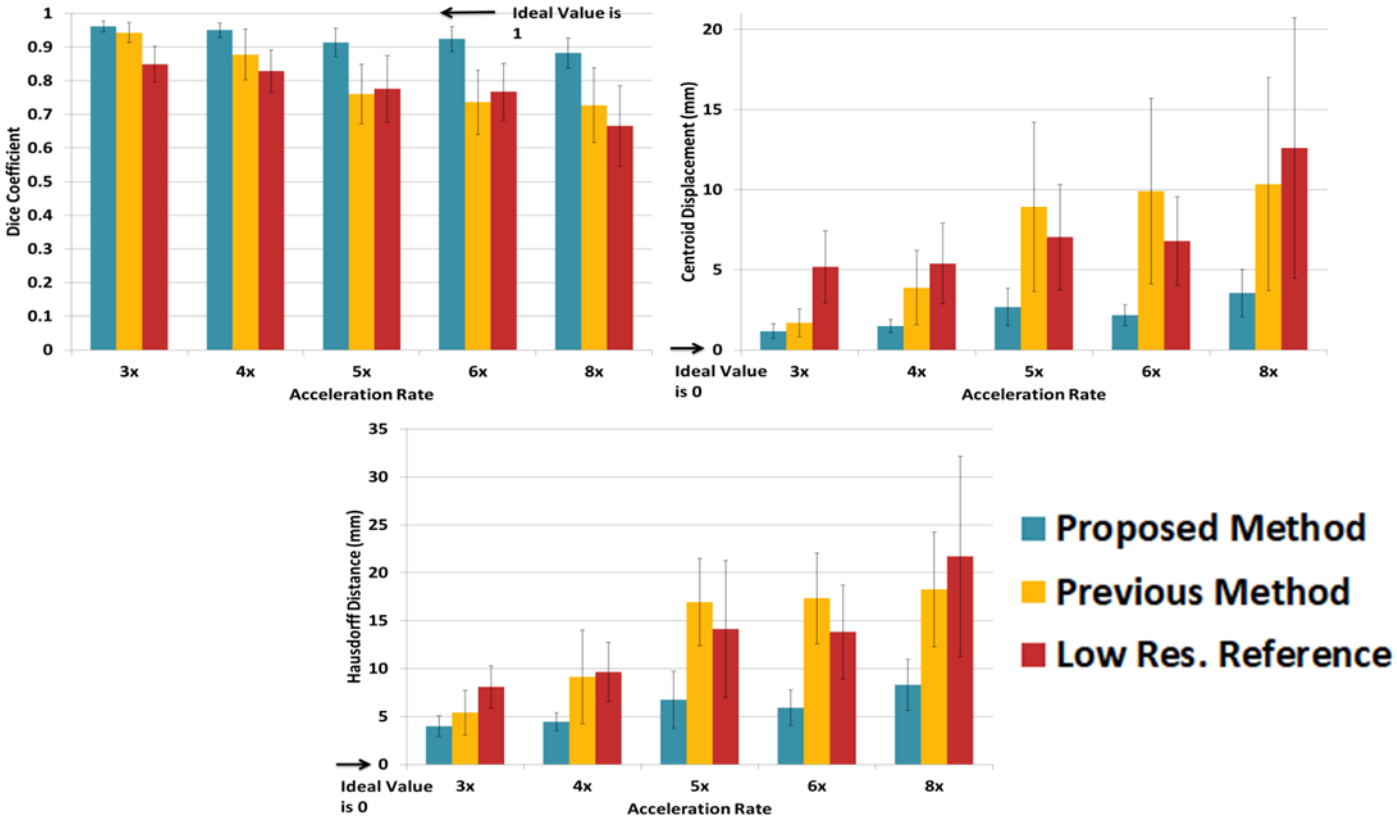

Figure 2.10: Effects of acceleration rate on a) Dice coefficient, b) Centroid displacement and c) Hausdorff distance, using our proposed method. Displayed are averages from all patient data sets using the optimal number of PCs for fitting as identified during testing. A comparison was also performed with the previous method by Dietz et al. Statistics from a low-resolution acquisition of an equivalent acceleration rate are also included for reference.

Figure 2.11 provides further detail into the effects of the number of principal components used for fitting over various acceleration rates. The same number of principal components used for fitting per acceleration rate was kept consistent with the image quality tests represented by Figure 2.4.

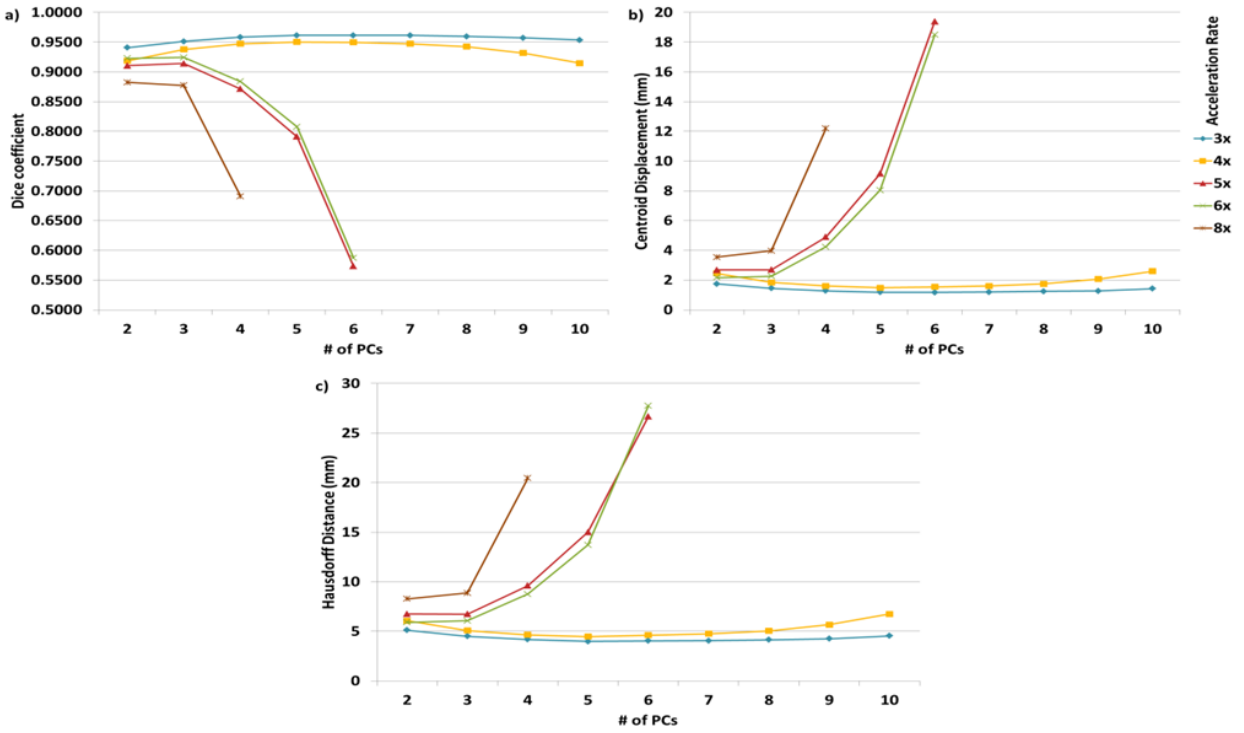

Figure 2.11: Total patient average a) Dice coefficient, b) Centroid Displacement and c) Hausdorff Distance as a function of the number of PCs kept for reconstruction and acceleration rate. Each line represents a different acceleration rate.

2.5 Discussion

2.5.1 Core size and N_{COMP} selection

The two best-performing and two worst-performing patient data sets in terms of NMSE, SSIM, and PSNR at an acceleration factor of 3x were selected to test various combinations of core size and N_{COMP} that created acceleration factors ranging up to 8x. Once a particular combination was chosen for a specific acceleration rate, it was then run on all fifteen patients to fully test the method's capabilities at a particular acceleration. The maximum core size that was tested was sixteen and the minimum core size tested was eight. There is a trade-off when determining the size of the core; if it is larger, then fewer outer k-space points can be acquired which can lead to less information and greater instability for fitting. If it becomes too small the PCs will be calculated from a small database which can lead the PCs to be less representative of the range of changes that are occurring in the outer k-space.

2.5.2 Effects of N_{PC} on image reconstruction

For lower acceleration rates, using N_{PC} values of four or five was optimal to get the best image reconstruction quality. As N_{PC} increased noise artifacts became more prevalent and degraded the image quality when looking at the time evolution of the method. Further investigation is needed to determine the best way to suppress these noise spikes, so that more PCs can be retained for fitting thus providing more motion detail. As the acceleration increased the optimum number of PCs for fitting became smaller, due to greater instability when fitting to more sparsely sampled data. Overall, the noise artifact increased with acceleration. However, by reducing the number of PCs for fitting, contourable images could still be derived at acceleration factors of up to 8x.

2.5.3 Temporal robustness

As shown in Figures 2.6a and b, the metrics representing image fidelity remain robust over time. Slight fluctuations are likely caused by uncertainties in the fitting process possibly derived from the small number of sampled points across the reconstruction window. In comparison to the frame-based method, this technique shows much more stability over time, albeit with a sacrifice in initial quality. This can further be seen in Figure 2.6c which compares the final frame reconstructed with the two different methods. A comparison is also displayed between the final frame of our method to the same frame of the fully-sampled data, as well as to the same data set which was retrospectively acquired with only the central third of k-space and reconstructed using a standard Fourier transform. In order to correspond to an acceleration of 3x, k-space was divided into thirds and only the central data was acquired to mimic a low-resolution acquisition for reference. Qualitatively, our method (Figure 2.6c, Proposed Method) did not perform as well as the fully-sampled image (Figure 2.6c, Fully Sampled), which is to be expected. However, it did provide less blur and more image detail than only acquiring the central k-space data (Figure 2.6c, Low Res. Reference). This is quantified in Figures 2.8 and 2.10 through imaging and contouring metrics. Figure 2.7 shows that over an imaging session the metrics used remain relatively constant over time whereas for the Dietz et al. method the metrics degrade over time, sometimes quite rapidly.

2.5.4 Comparison to other methods

When comparing this proposed method with that of Dietz et al. at higher acceleration factors, it appears our proposed method provides an overall advantage until an acceleration factor of 8x, at which point the SSIM falls lower, although the NMSE and PSNR remain better (Figure 2.8). Further comparisons were done to low resolution acquisitions equivalent to each acceleration rate. Figures 2.8 and 2.10 demonstrate that using our reconstruction method provides better quality images and contours than a simple low resolution acquisition. In the paper written by Dietz et al. they compare their method to a standard Compressed Sensing technique and demonstrated their method worked better.[11] This suggests that our method would likely perform better than that compressed sensing implementation.

2.5.5 Contour-based analyses

Auto-contouring of the target tumor is an important part of the Linac-MR as real-time imaging produces too many images at too quick a rate for a radiation oncologist to keep up and maintain the real-time nature of the process, so it is important that our proposed method produces images at a good enough quality to work with the auto-contouring software. Six patients used in previous contouring studies within our group were used to test contour ability of our reconstructed images.[11,15] The target tumors of interest were all lung tumors and ranged in cross-sectional size from 1.4-5.0cm^2.[24] Tumour size and shape did not appear to play a significant role in the ability to accurately contour. The effects of acceleration rate and the number of principal components kept for reconstructed were tested using Dice coefficient, Hausdorff distance and centroid displacement. Overall, our method shows higher Dice coefficient values, while also maintaining lower contour displacement, as measured with centroid displacement and Hausdorff distance, when compared to the previous method by Dietz et al.

At acceleration rates of 3x and 4x it appears that four to five PCs for fitting provided the best images for reconstruction. At accelerations of 5x and 6x the number used for fitting drops to two or three PCs and for an acceleration of 8x the number of PCs drops to only two. This is somewhat expected due to greater fitting instability as less data is acquired at higher acceleration rates. Noise artifact from this fitting instability can throw off the auto countering software which can lead to a poor contour or not being able to contour the image at all.

2.5.6 Limitations and Future Work

The incoherent noise spikes at higher values of PCs limits the number of PCs used for fitting and therefore limits the amount of motion detail we can reconstruct. This can be seen with the Dice coefficient plots vs N_{PC} in Figure 2.11 in which the values initially increase with N_{PC}, but then decline as more noise artifact is introduced, nulling the detail gains. Adjustments in the acceleration method algorithm will need to be made if more motion detail is desired in the future.

Each patient, used to test the contouring capabilities of the method, resulted in 591 reconstructed frames, giving a total of 3546 frames for a given N_{PC} value, at each acceleration rate. During this testing it was found that the auto-contouring software was not able to distinguish a contourable ROI on certain frames. Upon inspection, the frames for which contouring failed had a large amount of artifact that was introduced into the reconstruction which caused some anatomic structures to become indistinguishable. As shown in Table 2.2 this problem generally only became an issue as the value of N_{PC} was pushed too far. This issue affected certain patients more than others. Further, it can be seen that at each acceleration factor, the parameters can be optimized for consistent success in contouring. Future work will need to be done to ensure success for all a greater range of options. Table 2.2 represents the number of uncontourable frames as a function of acceleration rate and N_{PC}.

Table 2.2: Total number of uncontourable frames over six total patients (total of 3546 frames) as a function of PCs kept for reconstruction and acceleration rate

	N_{PC} (Number of PCs employed for reconstruction)								
Acceleration Rate	**2**	**3**	**4**	**5**	**6**	**7**	**8**	**9**	**10**
3x	0	0	0	0	0	0	0	0	0
4x	0	0	0	0	0	0	0	0	2
5x	0	1	3	16	34	-	-	-	-
6x	0	1	2	14	21	-	-	-	-
8x	1	5	24	-	-	-	-	-	-

One of the next steps in testing will be acquiring prospectively undersampled data from the Linac-MR system. While the retrospective approach allows for assessment compared to the fully-sampled gold standard, acquisition of prospectively undersampled data can introduce artifacts and will need to be investigated. Further work will also need to be done to determine the cause of the spikes of uncertainty at higher N_{PC} values. This is likely the cause for the uncontourability of certain frames at higher N_{PC} values due to reduced image quality. Being able to increase the number of PCs employed for reconstruction may lead to better image quality by better characterizing the motion detail. Utilizing previously fully-reconstructed frames into the reconstruction of future frames may be one way of handling these noise spikes, by reducing degrees of freedom in the fitting process and thereby improving stability, and is a potential area for future work. Optimizing the size of the reconstruction window could be another solution. A smaller window may be able to better represent the current state of the anatomy in question and handle sudden changes. Alternatively, a bigger window may be needed in order to better average out sudden changes. In future work this parameter should be subjected to optimization in order to maximize stability of the algorithm.

The retrospective analysis performed in this study was done on combined data in order to simulate a single channel. It is our plan in future to explore how this algorithm may be best integrated into a multi-channel data set, for example whether it is best to reconstruct each with the algorithm separately, or somehow combine the algorithm to operate on the data set as a whole. However, we feel this is beyond the scope of this current work.

2.6 Conclusions

A computationally inexpensive real-time 2D accelerated MRI method using time domain PCA requiring limited hardware (i.e., a simple receive coil and limited computing power) was developed and tested using fifteen fully-sampled patient data sets. It was found that this method provides good temporal robustness provided optimal parameters are chosen. Using image quality metrics such as NMSE, PSNR, Dice coefficient and Hausdorff distance, it was found that this method can provide real-time accelerated data acquisition and reconstruction, which can be contoured with a similar accuracy to that of an equivalent fully-sampled image, up to an acceleration factor of 8x. The algorithm did not require extra coil hardware, meaning it can be run with simple single coil channel setups. It was found that reconstruction of raw acquired data

can be performed at roughly 50ms per frame (Intel® Core i5-2430M CPU @ 2.40GHz, 6GB RAM).

2.7 References

1. Fallone, BG., Murray, B., Rathee, S., et al., First MR images obtained during megavoltage photon irradiation from a prototype integrated linac-MR system. *Medical Physics*, 2009;36(6):2084-2088.
2. Winkel D, Bol GH, Kroon PS., et al., Adaptive radiotherapy: The Elekta Unity MR-linac concept. *Clinical and Translational Radiation Oncology*. 2019;18:54-59.
3. Keall PJ, Barton M, Crozier S. The Australian Magnetic Resonance Imaging–Linac Program. *Seminars in Radiation Oncology*. 2014;24(3):203-206.
4. Klüter S. Technical design and concept of a 0.35 T MR-Linac. *Clinical and Translational Radiation Oncology*. 2019;18:98-101.
5. Yip E, Yun J, Wachowicz K, et al. Prior data assisted compressed sensing: A novel MR imaging strategy for real time tracking of lung tumors. *Medical Physics*. 2014;41(8):082301.
6. Uecker M, Zhang S, Voit D, Merboldt K-D, Frahm J. Real-time MRI: recent advances using radial FLASH. *Imaging in Medicine*. 2012;4(4):461-476.
7. Brix L, Ringgaard S, Sørensen TS, Poulsen PR. Three-dimensional liver motion tracking using real-time two-dimensional MRI. *Medical Physics*. 2014;41(4):042302.
8. Kim T, Park JC, Gach HM, Chun J, Mutic S. Technical Note: Real-time 3D MRI in the presence of motion for MRI-guided radiotherapy: 3D Dynamic keyhole imaging with super-resolution. *Medical Physics*. 2019;46(10):4631-4638.
9. Terpstra ML, Maspero M, D'Agata F, et al. Deep learning-based image reconstruction and motion estimation from undersampled radial k-space for real-time MRI-guided radiotherapy. *Physics in Medicine & Biology*. 2020;65(15):155015.
10. Yip E, Yun J, Wachowicz K, Gabos Z, Rathee S, Fallone BG. Sliding window prior data assisted compressed sensing for MRI tracking of lung tumors. *Medical Physics*. 2017;44(1):84-98.

11. Dietz B, Yip E, Yun J, Fallone BG, Wachowicz K. Real-time dynamic MR image reconstruction using compressed sensing and principal component analysis (CS - PCA): Demonstration in lung tumor tracking. *Medical Physics*. 2017;44(8):3978-3989.
12. Wang F, Hennig J, Levan P. Time-domain principal component reconstruction (tPCR): A more efficient and stable iterative reconstruction framework for non-Cartesian functional MRI. *Magnetic Resonance in Medicine*. 2020;84(3):1321-1335.
13. Pedersen H, Kozerke S, Ringgaard S, Nehrke K, Kim WY. k-t PCA: Temporally constrained k-t BLAST reconstruction using principal component analysis. *Magnetic Resonance in Medicine*. 2009;62(3):706-716.
14. Petzschner FH, Ponce IP, Blaimer M, Jakob PM, Breuer FA. Fast MR parameter mapping using k-t principal component analysis. *Magnetic Resonance in Medicine*. 2011;66(3):706-716.
15. Yun J, Yip E, Gabos Z, Wachowicz K, Rathee S, Fallone BG. Neural-network based autocontouring algorithm for intrafractional lung-tumor tracking using Linac-MR. *Medical Physics*. 2015;42(5):2296-2310.
16. Bi X, Park J, Deshpande V, Simonetti O, Laub G, Li D. Reduction of flow- and eddy-currents-induced image artifacts in coronary magnetic resonance angiography using a linear centric-encoding SSFP sequence. *Magnetic Resonance Imaging*. 2007;25(8):1138-1147.
17. PCA. Principal component analysis of raw data - MATLAB. https://www.mathworks.com/help/stats/pca.html. Accessed March 15, 2021.
18. Penrose R. A generalized inverse for matrices. *Mathematical Proceedings of the Cambridge Philosophical Society*. 1955;51(3):406-413.
19. Peak Signal-to-Noise Ratio as an Image Quality Metric. NI. https://www.ni.com/en-ca/innovations/white-papers/11/peak-signal-to-noise-ratio-as-an-image-quality-metric.html. Accessed March 15, 2021.
20. Wang Z, Bovik A, Sheikh H, Simoncelli E. Image Quality Assessment: From Error Visibility to Structural Similarity. *IEEE Transactions on Image Processing*. 2004;13(4):600-612.
21. SSIM. Structural similarity (SSIM) index for measuring image quality - MATLAB. https://www.mathworks.com/help/images/ref/ssim.html. Accessed March 15, 2021.

22. Dice. Sørensen-Dice similarity coefficient for image segmentation - MATLAB. https://www.mathworks.com/help/images/ref/dice.html. Accessed March 15, 2021.
23. Ngan KN, Meier T, Chai D. Video Object Plane Extraction and Tracking. *Advanced Video Coding: Principles and Techniques Advances in Image Communication*. 1999:251-314.
24. Dietz B, Yun J, Yip E, Gabos Z, Fallone BG, Wachowicz K. Single patient convolutional neural networks for real-time MR reconstruction: a proof of concept application in lung tumour segmentation for adaptive radiotherapy. *Physics in Medicine & Biology.* 2019:65:195002.

Chapter 3
Effects of Added Noise

3.1 Introduction

In MRI, the signal to noise ratio (SNR) is an important factor when attempting to acquire and reconstruct quality images. SNR is simply the amount of signal present in the image divided by the noise level of the image (Equation 3.1).

$$SNR = \frac{MR\ Signal}{Noise}. \qquad (3.1)$$

The amount of signal available, in MRI, changes proportionally with the square of the B_o field strength.[1] This is caused by the increase in polarization at higher field strengths as well as the increase in frequency of the precession. Increasing the polarization will result in an increased number of magnetic moments pointing in the direction of the B_o field. An increase in the frequency of precession (correlating with B_0) will produce a linear increase in the rate of change of the magnetic flux. Due to Faraday's Law, in a wire loop, this will cause a linear response in the induced emf in the coil increasing the amount of signal available.[1]

The amount of noise is dependent on the frequency of the system. At low frequencies (low field strengths) the noise is dominated by the electronics and coils of the system. This causes the noise to have a $B_o^{1/4}$ dependency.[1] As the frequency increases the noise starts to become dominated by the sample which is being imaged. This noise has a linear B_o dependence.[1] Most clinical field strengths are found in this linear response region. Models have predicted that for field strengths greater than or equal to 0.5T, the deviation from the linear response will be no more than 6.3%, with the maximum deviations occurring around 0.5T.[1] There are many other factors that can affect SNR in an MR system. These factors include sample conductivity and sample size, coil choice, size or arrangement as well as acquisition time, spatial resolution, relaxation times and proton density.[2]

From equation 3.1, and assuming the noise is sample dominated, it can be seen that SNR will change linearly with a change in B_o. For this work a 100% linear response was assumed for all noise levels.

$$SNR \propto \frac{B_o^2}{B_o} \propto B_o. \quad (3.2)$$

As discussed different field strengths result in different SNR levels. Additionally different MR sequences can also produce different SNR levels. Testing the method at different noise levels will demonstrate its limits when faced with changing SNR levels in the real world. Poor coil placement, external noise sources and other unforeseen circumstances can arise during an imaging session which can change the SNR. It is important to show that the method can handle these sudden changes in SNR and still maintain acceptable images.

In this study the effects of added noise was tested on the through-frame PCA algorithm at noise levels of N = 2, 4 and 6 when compared to the original 3T data at acceleration rates ranging from 3x to 8x. The through-frame PCA method utilizes a sliding reconstruction window in order to fully-reconstruct the final frame of the window. PCA is performed on a core set of phase encodes located in central k-space. Outside of this core, the phase encodes are undersampled. This undersampled data is mulitplied with the calculated PCs to generate weights. These weights are multiplied with the PCs calculated from the frame of interest and the acquired data from that frame in order to fill in the missing data and fully-reconstruct the frame.

3.2 Methods

In order to test the effects of low SNR on our algorithm, random complex noise was added to the original 3T data at N=2, 4 and 6 times the noise of the original fully-sampled image. The standard deviation of the added noise was calculated such that:

$$\sigma_{added} = \sqrt{N^2 - 1}\sigma_{measured}. \quad (3.3)$$

$\sigma_{measured}$ was calculated on the real and imaginary channels of the complex image domain data by selecting an image region of interest free of any signal or streaking artifact. Figure 3.1 provides an example of the location and size of the region of interest selected to measure the initial noise level of the image.

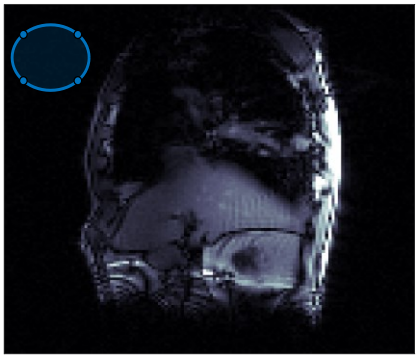

Figure 3.1: A visual representation of a region of interest used to measure the initial noise level of an image

The measured standard deviation was averaged over all the dynamic frames within the data set. The appropriate standard deviation of added noise was then calculated using equation 3.3 and used to generate a matrix of complex noise with a gaussian distribution the same size as the image data matrix. This was then converted to the k-space domain using a Fourier transform for addition with the original k-space data. Added noise multiples of $N = 2$, 4 and 6 were evaluated. This testing was performed on the six data sets used to test the contouring capabilities for the original data.

After reconstruction the accelerated images were analyzed for image quality using Normalised Mean Square Error (NMSE), Structural Similarity Index (SSIM) and peak-SNR (PSNR). This was done by comparing the noise added accelerated reconstructions to the original fully-sampled data with no noise added. To investigate the trends of these metrics with regard to SNR, the results were compared between each of the noise levels. The accelerated images at N=1 were also included for comparison. A total of six data sets from non-small cell lung cancer patients were used to test the algorithm.

The accuracy of the generated contours, drawn using auto-contouring software developed by our group, was measured using the metrics; Dice coefficient, Hausdorff distance and centroid displacement.[3] The contours were compared with those from the fully-sampled no noise added data, which was considered the gold standard. As with the image quality metrics, the accelerated images at N=1 were included for comparison.

The previous testing yielded metrics which included the noise distribution as well as the effects from acceleration, due to the reconstructed images being compared to a no noise added image. In order to strictly test the effects of acceleration on the method we performed a second series of

evaluations in which the reconstructed images were compared to the same fully-sampled data sets with noise added. The noise was added to the fully-sampled data sets in the same manner as described above. In order to eliminate differences due to changes in noise pattern, these noise-added, fully-sampled data sets were then undersampled (using the same undersampling patterns as above) and reconstructed using the reconstruction code with the same optimal N_{PC} values. The reconstructed images were then compared to the fully-sampled data sets of the same noise level using the same image quality and contour metrics described above.

3.3 Results and Discussion

Figure 3.2 demonstrates the effects of added noise of image quality metrics NMSE, PSNR and SSIM at each noise level and for all acceleration rates tested.

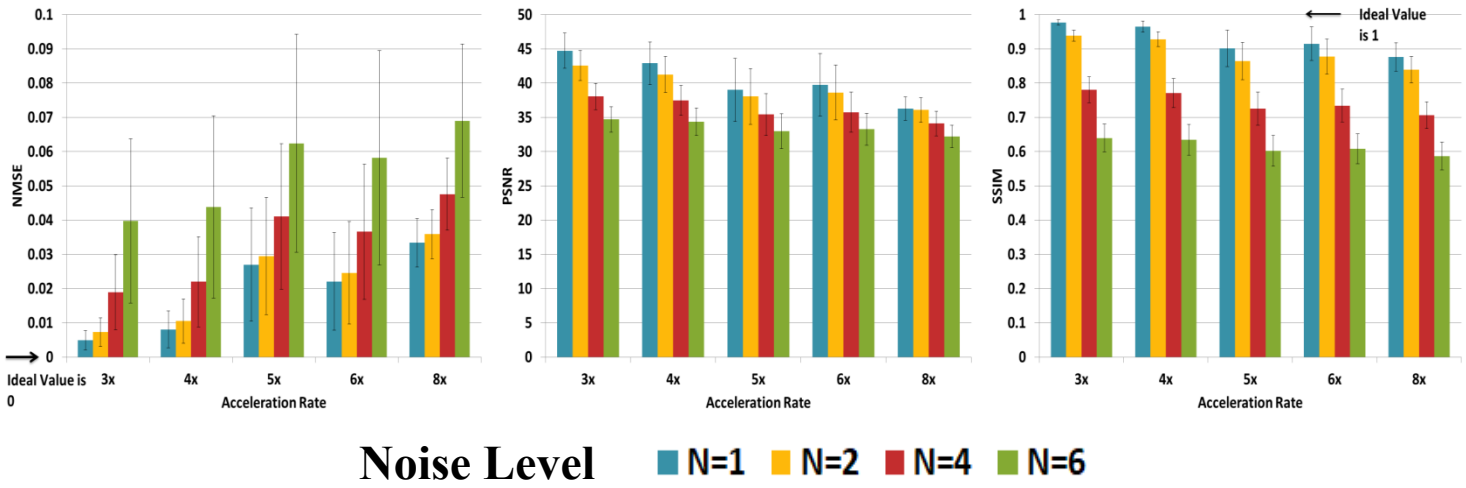

Figure 3.2: A comparison of image quality metrics (NMSE, PSNR and SSIM) at noise levels of N = 1,2,4 and 6 and at acceleration rates of 3x, 4x, 5x, 6x and 8x.

As shown in Figure 3.2, the addition of extra noise has a noticeable effect on NMSE and SSIM causing a large amount of variation while also having a smaller effect on PSNR.

While image quality metrics (NMSE, PSNR and SSIM) are important for measuring image fidelity, the primary function of this real-time imaging application will be to accurately identify and track image structures. Figure 3.3 demonstrates a comparison of contour statistics (Dice coefficient (overlap of the reconstructed with the gold standard contour), Hausdorff distance (greatest distance from a point in one data set to its nearest point in the other data set) and

centroid displacement (distance between the centroid of one contour to that of the other contour)) over different noise levels and acceleration rates.

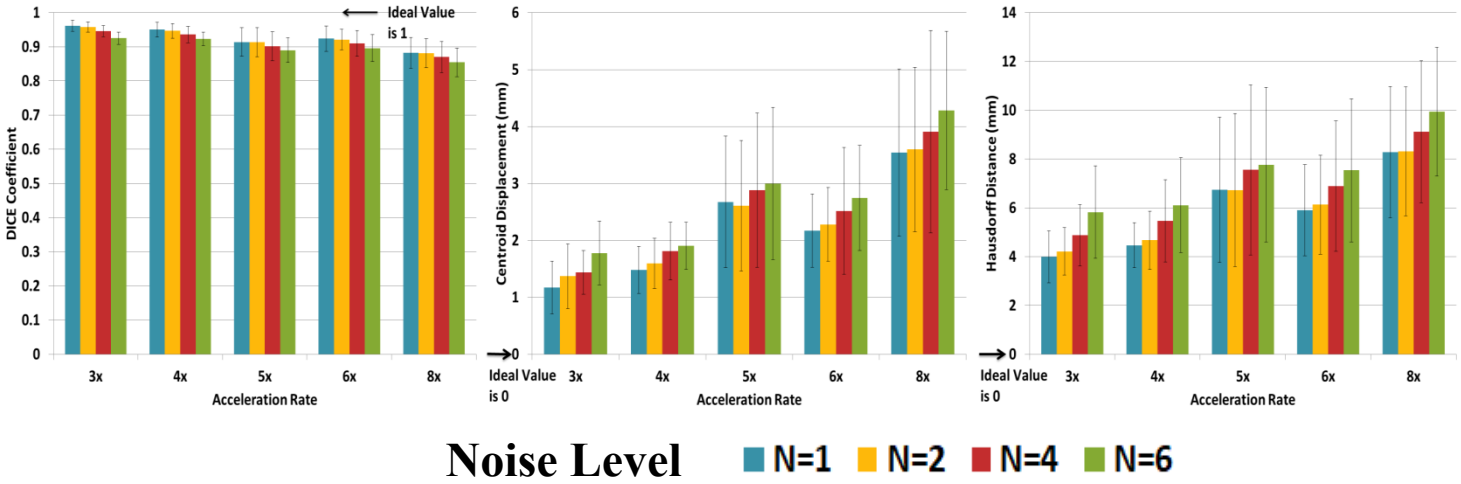

Figure 3.3: A comparison of contourability metrics (Dice coefficient, Hausdorff distance and centroid displacement) at noise levels of N = 1, 2, 4 and 6 and at acceleration rates of 3x, 4x, 5x, 6x, and 8x.

Figure 3.3 shows that there is less variation in contourability metrics, particularly the Dice coefficient, between noise levels at a given acceleration rate when compared to the image quality metrics in Figure 3.2. This is important as real-time imaging for radiation therapy will primarily be used to track and contour structures of interest and in this context is more important than image quality metrics.

Figure 3.4 is a visual representation of the effects of added noise on the images. For this work noise added levels of N = 2, 4 and 6 were tested. The standard N = 1 level is also shown as a reference.

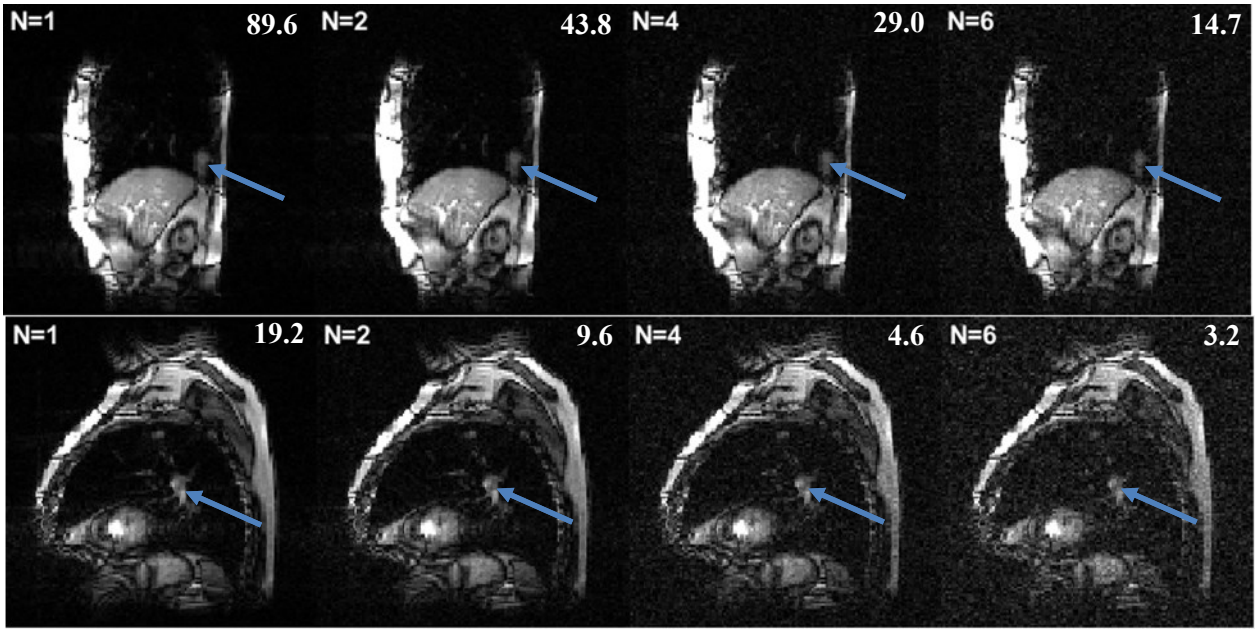

Figure 3.4: A visual representation of the reconstructed images at each noise level at acceleration of 4x with an N_{PC} value of 5. A reconstructed image from noise level N=1 is shown as a reference. The position of the tumour in each image is also highlighted. SNR values for each image are displayed in the top right corner. Each row represents a different patient.

The increased noise is apparent in the images in Figure 3.4, corresponding to the added noise to the k-space data. Despite this, it appears that decreased SNR by itself does not have a destructive effect on the algorithm as it continues to reconstruct the undersampled data with correspondingly noisier outputs.

Figure 3.5 demonstrates the effects of SNR level on the optimization of the number of PCs used for reconstruction (N_{PC}) using SSIM and Dice coefficient for acceleration rates of 4x, 6x and 8x. A comparison is made between each noise level including the original N=1 reconstructed data.

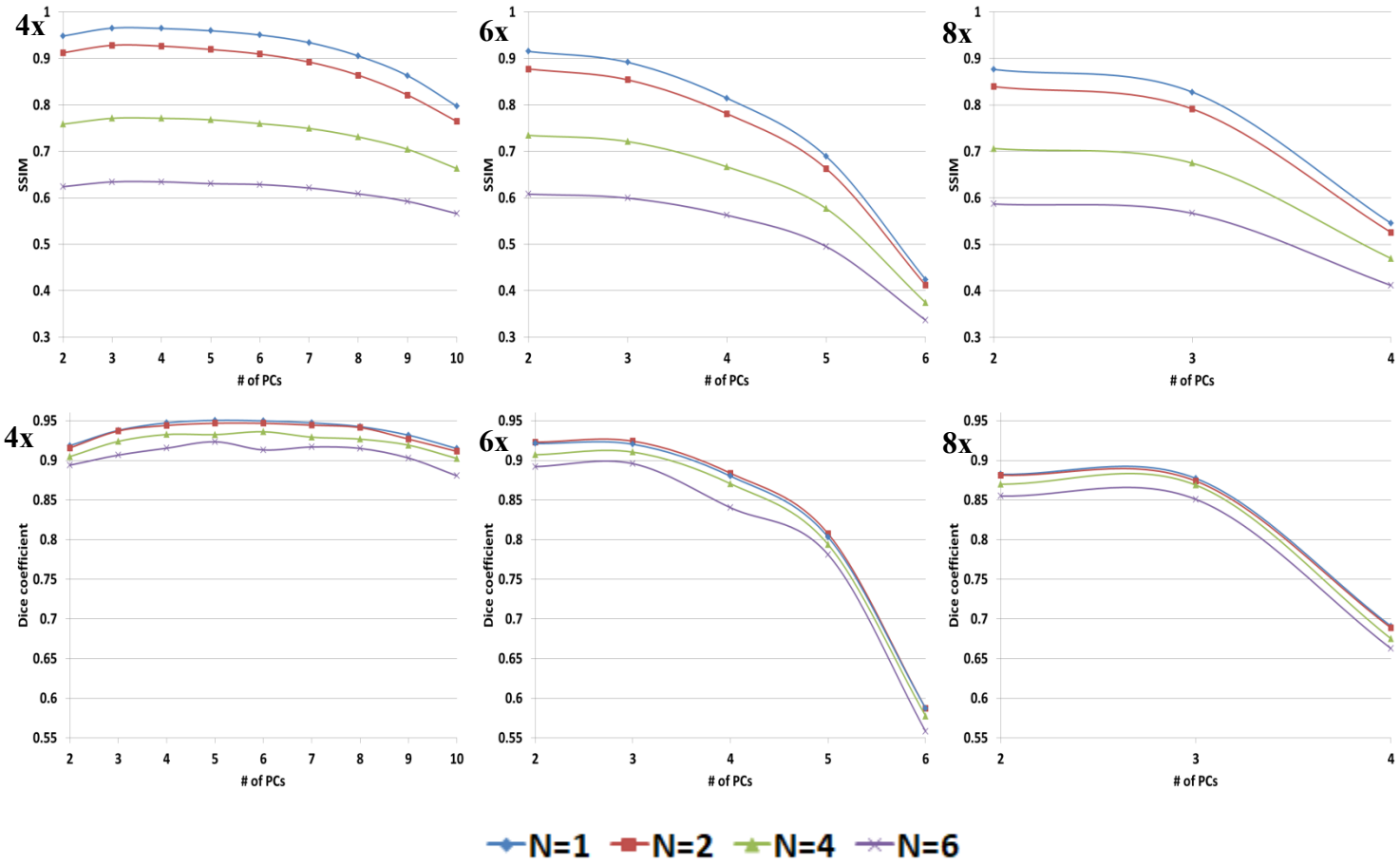

Figure 3.5: The effects of the number of PCs kept for reconstruction on SSIM and Dice coefficient at different noise levels. Acceleration rates of 4x, 6x and 8x are displayed. The value at each noise level is the average value of the six patients used in the study.

Figure 3.5 is a comparison of the effect of the number of PCs kept for reconstruction on SSIM and Dice coefficient at the different noise levels. Similar trends can be seen at each noise level meaning that minimal changes in parameters for reconstruction will be needed when the algorithm is used at different noise levels. The number of PCs used for fitting is an important metric in the optimization of this method. More PCs will allow for greater motion detail in the image; however, the tradeoff is that more noise is introduced to the image. Optimization is

needed in order to have enough temporal detail in the images without overwhelming them with too much noise.

Figure 3.5 demonstrates that the evolution of metrics with N_{PC} follow the same pattern regardless of SNR level. This is important because once the parameters have been optimized for a particular undersampling pattern and acceleration rate, they will require no or minimal changes when used at different noise levels. It also shows that the algorithm should be able to withstand sudden changes in SNR during an imaging session, while parameters associated with the acceleration implementation will remain valid.

Figure 3.6 is a comparison of image quality and contour metrics over a range of acceleration rates for a particular range of noise levels. For this comparison, the reconstructed images were compared against a fully-sampled data set of the same noise level and to contours generated on these added noise fully-sampled data sets.

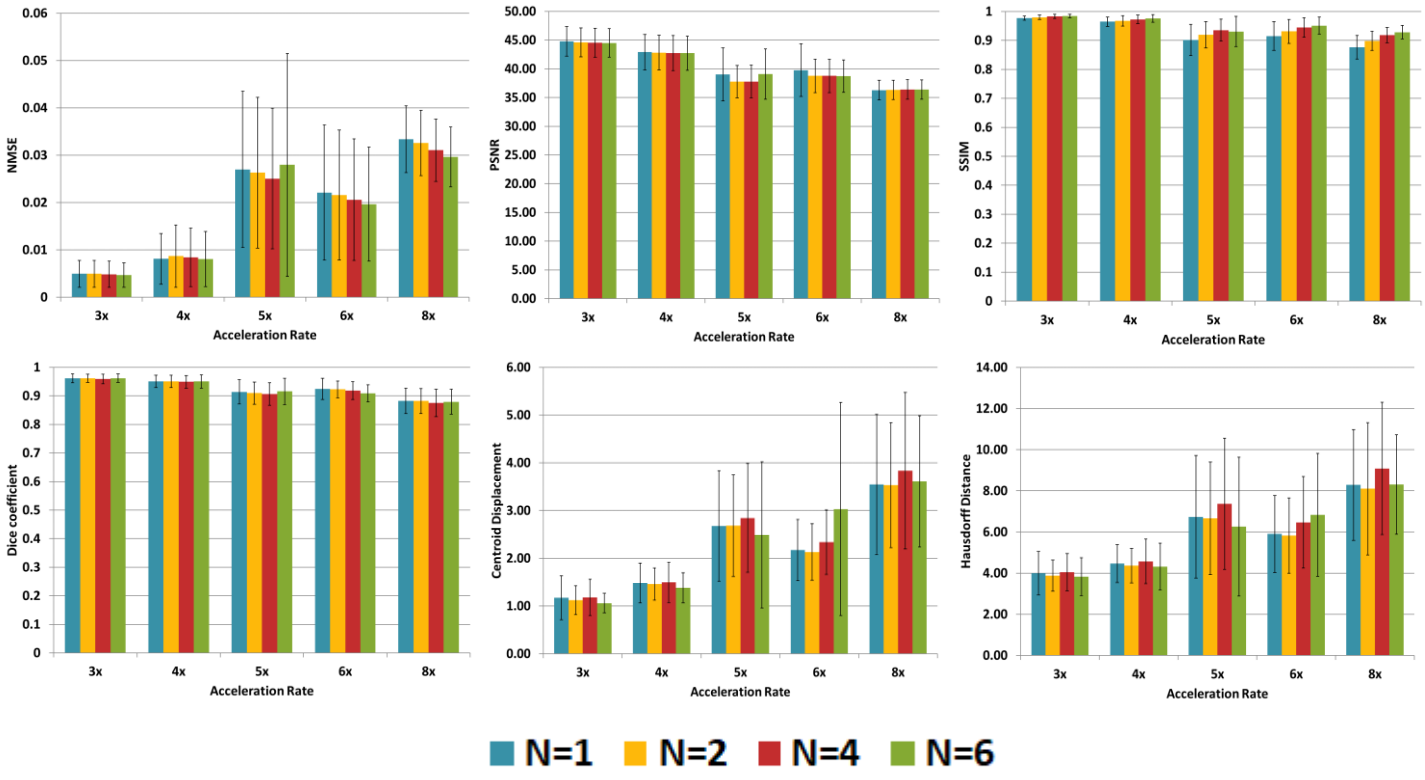

Figure 3.6: A comparison of image quality and contour metrics over a range of acceleration rates at different noise levels.

Figure 3.6 demonstrates that the method appears to be robust against added noise. This can be seen in each of the metrics as they appear to remain similar, within measurement error, for a

particular acceleration rate as the noise level is increased. Figure 3.6 also shows that acceleration rate affects the method in a similar manner to the no noise added data. This is to be expected and appears to have only minor effects on metrics such as PSNR, SSIM and Dice coefficient.

These are important results as they demonstrate the robustness of the method as the SNR level decreases and that higher acceleration rates even at low SNR levels have a limited effect on the method. From these results it appears our method will acquire and reconstruct images of acceptable quality, for its intended purpose of structure tracking, at low SNR levels, consistent to what is found at 0.5T, at acceleration rates up to 8x.

Planned future work includes prospective acquisition on the 0.5T Linac-MR system developed at the Cross Cancer Institute. This will provide a more accurate representation of how the method works at low field strength as noise and signal are not the only things that change when field strength changes. It will show the effects of different T1 and T2 times found at lower field strengths and changes to contrast to noise ratio on image quality.

3.4 Conclusions

The effect of additional noise on the algorithm was tested. Added noise does seem to have an effect of the image quality metrics (NMSE, PSNR and SSIM) but the contourability of each image (Dice coefficient, Hausdorff distance, centroid displacement), which is more important in a real-time auto-contouring environment, varied to a lesser extent as the amount of noise increased. When using a noise-added fully-sampled data set as the gold standard for comparison, the algorithm appears to be robust to the different noise levels that were tested. Acceleration did appear to degrade the metrics, although this is to be expected and appears to be no different than the case with no noise added. At each noise level at the various acceleration rates, the trend in the number of PCs kept for reconstruction, in terms of SSIM and Dice coefficient, were similar for each noise level. This means that at each noise level the same number of PCs used for reconstruction in order to produce the best results is similar and there would be a minimal need for changes in parameters when the algorithm is used at different noise levels.

While prospective analysis at lower field strengths will ultimately show how the algorithm performs with added noise, this retrospective analysis has provided a general idea of how the algorithm will perform and shows promise when used in a reduced SNR environment.

3.5 References

1. Brown, R. W., Cheng, Y.-C. N., Haacke, E. M., Thompson, M. R., Venkatesan, R. (2014). *Magnetic resonance imaging: physical principals and sequence design*. John Wiley & Sons.

2. Nishimura D. G. (2016). "7.5 Noise considerations" in *Principles of Magnetic Resonance Imaging, www.lulu.com, 154-166.*

3. Yun, J., Yip, E., Gabos, Z., Wachowicz, K., Rathee, S., Fallone, B. G. (2015). Neural-network based autocontouring algorithm for intrafractional lung-tumor tracking using Linac-MR. *Med Phys*, 42(5), 2296-2310.

Chapter 4

Conclusions and Future Work

Real-time MR imaging is becoming increasingly utilized in conjunction with radiation therapy on hybrid Linac-MR systems. Real-time imaging can allow for adaptive radiation therapy where the beam is constantly being shifted in order to focus solely on the target. Using real-time imaging can allow for smaller margins to be used during treatment planning, meaning more healthy tissue will be spared from harmful radiation. This can be done by tracking the target and shaping the beam to conform to the target and even shut off the beam if the target moves out of range.

In order to have effective real-time imaging, accelerated low latency MR techniques are needed. The work presented in this thesis describes a potential acceleration method for on-the-fly real-time imaging. The method utilizes Principal Component Analysis (PCA) and undersampled k-space data in order to reconstruct a full image. Our method utilizes a core set of phase encodes in central k-space in order to calculate the Principal Components (PCs) which are representative of the temporal fluctuations of k-space over time and are consistently updated throughout an imaging session. Outside of this core the outer k-space data is undersampled using a set of complementary patterns. These complementary patterns ensure that all of k-space is acquired within a pre-determined number of frames. A reconstruction window of N_{WIN} frames is used to fully reconstruct the final frame of the window.

Chapter 1 of this thesis provided background information into external-beam radiation therapy as well as information on Linac-MR systems. It also demonstrated how PCs are calculated using PCA. Chapter 2 provided an in-depth explanation of how our proposed method works. The method was tested retrospectively on 15 fully-sampled 3T data sets using MatLab software (2020b, The MathWorks Inc., Natick MA, USA). Analysis was done on image quality using Normalised Mean Square Error (NMSE), Structural Similarity Index (SSIM) and peak-SNR (PSNR). The accelerated reconstructed images were compared to the original fully-sampled 3T data. Optimization was done in order to find the optimal number of PCs used for reconstruction

at each acceleration rate. Comparisons were made with a previous PCA method by Dietz et al. as well as a low resolution acquisition of equivalent acceleration rate.[1] Further to this, a subset of six patients was used to determine the contourability of the reconstructed images, using auto-contouring software developed by our group.[2] Dice coefficient, Hausdorff distance and centroid displacement were used to compare the contours generated on the accelerated reconstructed images to those developed on the original fully-sampled 3T data.

It was found that our method outperformed both the method by Dietz et al. and the low res. acquisition over the course of an entire imaging session up to an acceleration factor of 8x, where the differences between our method and Dietz's became negligible. It was found that at the beginning of an imaging session (the first 260 frames or so), the method proposed by Dietz et al. outperformed our proposed method, particularly in Dice coefficient and centroid displacement. However, as the number of frames acquired increased, the proposed method showed greater robustness as the metrics showed less degradation. It was found that the optimal number of PCs used in reconstruction varied with acceleration rate. For acceleration rates of 3x and 4x, 4 or 5 PCs was optimal whereas for acceleration rates of 5x and 6x, 3 PCs was optimal and for an acceleration rate of 8x, 2 PCs was optimal. The contourability of our images showed good agreement with those developed on the fully-sampled data. When optimal parameters are chosen the Dice coefficient was still found to be around 0.88 at an acceleration rate of 8x, while remaining greater than 0.9 for all other acceleration rates. An ideal value for Dice coefficient is 1.

Chapter 3 demonstrated how the method would handle lower SNR settings. Noise was added in multiples of 2, 4 and 6, to the fully-sampled 3T data, in order to simulate different SNR levels. The same subset of six patients used to determine the contourability without noise was again tested for image quality and contourability, using the same metrics as above. The accelerated reconstructed images were compared with the fully-sampled 3T data with no noise added and to fully-sampled data with noise added at an equivalent noise level.

It was found that the image quality metrics NMSE, SSIM and to a lesser extent PSNR did show degradation with increasing noise level. However, the contourability metrics, Dice coefficient, Hausdorff distance and centroid displacement, showed less degradation, particularly the Dice coefficient. This is important as the main purpose of this method will be to produce images that

are able to be contoured in a real-time setting whereas the actual image quality will play a lesser role. It was found that when optimizing the number of PCs used in reconstruction similar trends were found at each of the noise levels, including no noise added, at each of the acceleration rates. This means that when optimal parameters are found for a particular undersampling pattern and acceleration, minimal changes will be needed when moving between different field strengths and therefore different SNR levels. It also means that the method should be robust enough to handle sudden changes in SNR which may occur during an imaging session. Visually it was found that while the images at higher noise levels did appear noisier, the noise in the final reconstructed image was proportional to that which was initially added. From this result it can be seen that the algorithm will remain robust as changes in SNR occur and it will respond to changes in noise in a roughly proportional way.

For this work only patients with lung tumours were studied due to the wider range of motion you would find during a treatment session. While a lung tumour typically maintains a similar pattern of motion throughout, sudden changes such as a patient taking a deeper or shallower breath may occur. Investigation could be done in order to further validate the method. Additionally other anatomy could be studied such as liver, prostate, and bladder. While these tumours may have less periodic motion than a lung tumour, they are also susceptible to sudden movement due to various bodily functions.

Further work can be done in order to be able to utilize more PCs for reconstruction. More PCs would allow for more motion detail however using more PCs would also introduce more uncertainty to the system. Currently it was found that while more PCs produced similar or better results in terms of metrics, sudden noise spikes occur, producing images of unacceptable quality. Optimization of the size of reconstruction window could be one technique to handling these noise spikes. Further to this, utilizing the previous fully reconstructed frames into the reconstruction of the current frame is an area that could be investigated.

Currently all testing of the algorithm has been limited to retrospective analysis of fully-sampled 3T data. Prospective analysis will need to be done on different systems and field strengths. While SNR does change with field strength, it is not the only parameter which changes with field strength. Parameters such as T1 and T2 weighting along with contrast and CNR also change.

Prospective analysis at lower field strengths will give a more accurate representation of how the algorithm will work under these conditions.

The fully-sampled data sets mimicked a single coil acquisition. In reality the data was collected using multiple coils and combined together to form a single fully-sampled image. While an advantage of this method is that it only requires a single coil for acquisition, investigations into multi-coil setups could be made. Investigating when to utilize PCA during the reconstruction is one example of this. In a multi-coil setup, PCA could be performed on the data acquired by each coil and then combined after, or all the data could be combined first and then have PCA performed on it.

We have developed an accelerated, low-latency MR reconstruction method for use in on-the-fly real-time imaging. Reconstruction times were ~50ms per frame (Intel® Core i5-2430M CPU @ 2.40GHz, 6GB RAM). Advantages to this method include being able to run the algorithm with limited computing power along with only needing a single coil, avoiding the need for complex multi coil setups.

4.2 References

1. Dietz B, Yip E, Yun J, Fallone BG, Wachowicz K. Real-time dynamic MR image reconstruction using compressed sensing and principal component analysis (CS - PCA): Demonstration in lung tumor tracking. Medical Physics. 2017;44(8):3978-3989.

2. Yun, J, Yip, E, Gabos, Z, Wachowicz, K, Rathee, S, Fallone, B. G. (2015). Neural-network based autocontouring algorithm for intrafractional lung-tumor tracking using Linac-MR. Med Phys, 42(5), 2296-2310.

Bibliography

Berthelsen, A. K., Dobbs, J., Kjellén, E., et al. What's new in target volume definition for radiologists in ICRU Report 71? How can the ICRU volume definitions be integrated in clinical practice? *Cancer Imaging*, 2007;7(1):104-116.

Bi X, Park J, Deshpande V, Simonetti O, Laub G, Li D. Reduction of flow- and eddy-currents-induced image artifacts in coronary magnetic resonance angiography using a linear centric-encoding SSFP sequence. *Magnetic Resonance Imaging*. 2007;25(8):1138-1147.

Brix L, Ringgaard S, Sørensen TS, Poulsen PR. Three-dimensional liver motion tracking using real-time two-dimensional MRI. *Medical Physics*. 2014;41(4):042302.

Brown, R. W., Cheng, Y.-C. N., Haacke, E. M., Thompson, M. R., Venkatesan, R. (2014). *Magnetic resonance imaging: physical principals and sequence design*. John Wiley & Sons.

Canadian Cancer Society, *Canadian Cancer Statistics 2019*, https://cdn.cancer.ca/-/media/files/research/cancer-statistics/2020-statistics/canadian-cancer-statistics/res-cancerstatistics-canadiancancerstatistics-2019-en.pdf?rev=82dc3652fe3648988b9174ad4b397a24&hash=6D3186DF3AC76787C58EE95D1712033C. Accessed April 29, 2021.

Canadian Cancer Society, *Chemotherapy*, Canadian Cancer Society, https://www.cancer.ca/en/cancer-information/diagnosis-and-treatment/chemotherapy-and-other-drug-therapies/chemotherapy/?region=on. Accessed May 3, 2021.

Canadian Cancer Society, *External radiation therapy,* Canadian Cancer Society, https://www.cancer.ca/en/cancer-information/diagnosis-and-treatment/radiation-therapy/external-radiation-therapy/?region=on. Accessed May 3, 2021.

Canadian Cancer Society, *Internal radiation therapy*, Canadian Cancer Society, https://www.cancer.ca/en/cancer-information/diagnosis-and-treatment/radiation-therapy/internal-radiation-therapy/?region=on. Accessed May 3, 2021.

Canadian Cancer Society, *Side effects of surgery*, Canadian Cancer Society, https://www.cancer.ca/en/cancer-information/diagnosis-and-treatment/surgery/side-effects-of-surgery/?region=on. Accessed May 3, 2021.

Cleveland Clinic, *When Is Ultrasound Used vs. an MRI for Bone, Muscle and Joint Problems?*, https://health.clevelandclinic.org/when-is-ultrasound-used-vs-an-mri-for-bone-muscle-and-joint-problems/. Accessed June 21, 2021.

Davis, C. P. *CT Scan vs. MRI Differences between Machines, Costs, Uses.* (MedicineNet) https://www.medicinenet.com/ct_scan_vs_mri/article.html. Accessed June 22, 2021.

de Oliveira, C., Weir, S., Rangrej, J., et al. The economic burden of cancer care in Canada: a population-based cost study. *CMAJ Open*, 2018;6(1);E1-E10.

Department of Energy, *How a Particle Accelerator Works*, https://www.energy.gov/articles/how-particle-accelerators-work. Accessed May 3, 2021.

Dice. Sørensen-Dice similarity coefficient for image segmentation - MATLAB. https://www.mathworks.com/help/images/ref/dice.html. Accessed March 15, 2021.

Dietz B, Yip E, Yun J, Fallone BG, Wachowicz K. Real-time dynamic MR image reconstruction using compressed sensing and principal component analysis (CS - PCA): Demonstration in lung tumor tracking. *Medical Physics*. 2017;44(8):3978-3989.

Dietz B, Yun J, Yip E, Gabos Z, Fallone BG, Wachowicz K. Single patient convolutional neural networks for real-time MR reconstruction: a proof of concept application in lung tumour segmentation for adaptive radiotherapy. *Physics in Medicine & Biology*. 2019:65:195002.

Elekta, *Elekta Unity: Two worlds one future*, https://www.elekta.com/dam/jcr:3883d2d4-d9e7-449d-84e2-815532681287/Elekta-Unity-Brochure.pdf. Accessed June 25, 2021.

Elster, A. D. (2021). *Larmor Frequency*. (ELSTER LLC) http://mriquestions.com/why-at-larmor-frequency.html. Accessed May 6, 2021.

Fallone, B. G. The Rotating Biplanar Linac–Magnetic Resonance Imaging System. *Seminars in Radiation Oncology*, 2014;24:200-202.

Fallone, BG., Murray, B., Rathee, S., et al., First MR images obtained during megavoltage photon irradiation from a prototype integrated linac-MR system. *Medical Physics*, 2009;36(6):2084-2088.

Gruber, B., Froeling, M., Leiner, T., Klomp , D. W. RF Coils: A Practical Guide for Nonphysicists. *Journal of Magnetic Resonance Imaging*, 2018;48:590-604.

Journal of Medical Physics, *Figure 1: The internal target volume defined by ICRU 62*, https://www.jmp.org.in/viewimage.asp?img=JMedPhys_2017_42_3_101_214491_f1.jpg. May 5, 2021.

Keall PJ, Barton M, Crozier S. The Australian Magnetic Resonance Imaging–Linac Program. *Seminars in Radiation Oncology*. 2014;24(3):203-206.

Kim T, Park JC, Gach HM, Chun J, Mutic S. Technical Note: Real-time 3D MRI in the presence of motion for MRI-guided radiotherapy: 3D Dynamic keyhole imaging with super-resolution. *Medical Physics*. 2019;46(10):4631-4638.

Klüter S. Technical design and concept of a 0.35 T MR-Linac. *Clinical and Translational Radiation Oncology*. 2019;18:98-101.

Lamey, M., Burke, B., Blosser, E., Rathee, S., De Zanche, N., Fallone, B. G. Radio frequency shielding for a linac-MRI system. *Physics in Medicine and Biology*, 2010;55:995-1006.

Ngan KN, Meier T, Chai D. Video Object Plane Extraction and Tracking. *Advanced Video Coding: Principles and Techniques Advances in Image Communication*. 1999:251-314.

Nishimura D. G. (2016). "7.5 Noise considerations" in *Principles of Magnetic Resonance Imaging, www.lulu.com, 154-166.*

PCA. Principal component analysis of raw data - MATLAB. https://www.mathworks.com/help/stats/pca.html. Accessed March 15, 2021.

Peak Signal-to-Noise Ratio as an Image Quality Metric. NI. https://www.ni.com/en-ca/innovations/white-papers/11/peak-signal-to-noise-ratio-as-an-image-quality-metric.html. Accessed March 15, 2021.

Pedersen H, Kozerke S, Ringgaard S, Nehrke K, Kim WY. k-t PCA: Temporally constrained k-t BLAST reconstruction using principal component analysis. *Magnetic Resonance in Medicine*. 2009;62(3):706-716.

Penrose R. A generalized inverse for matrices. *Mathematical Proceedings of the Cambridge Philosophical Society*. 1955;51(3):406-413.

Petzschner FH, Ponce IP, Blaimer M, Jakob PM, Breuer FA. Fast MR parameter mapping using k-t principal component analysis. *Magnetic Resonance in Medicine*. 2011;66(3):706-716.

SSIM. Structural similarity (SSIM) index for measuring image quality - MATLAB. https://www.mathworks.com/help/images/ref/ssim.html. Accessed March 15, 2021.

StackExchange. *Making sense of principal component analysis, eigenvectors & eigenvalues*. https://stats.stackexchange.com/questions/2691/making-sense-of-principal-component-analysis-eigenvectors-eigenvalues. Accessed August 19, 2021.

St. Aubin, J., Santos, D. M., Steciw, S., Fallone, B. G. Effect of longitudinal magnetic fields on a simulated in-line 6 MV linac. *Medical Physics*, 2010;37(9):4916-4923.

St. Aubin, J., Steciw, S., Fallone, B. G. Waveguide detuning caused by transverse magnetic fields on a simulated in-line 6 MV linac. *Medical Physics*, 2010;37(9):4751-4754.

Terpstra ML, Maspero M, D'Agata F, et al. Deep learning-based image reconstruction and motion estimation from undersampled radial k-space for real-time MRI-guided radiotherapy. *Physics in Medicine & Biology*. 2020;65(15):155015.

Tsang, D. S., Patel, S. Proton beam therapy for cancer. *CMAJ*, 2019;191(24):E664-E666.

Uecker M, Zhang S, Voit D, Merboldt K-D, Frahm J. Real-time MRI: recent advances using radial FLASH. *Imaging in Medicine*. 2012;4(4):461-476.

University Hospitals Plymouth, *Electron Beam Radiotherapy*, NHS, https://www.plymouthhospitals.nhs.uk/electron-beam-radiotherapy#:~:text=Electron%20beam%20radiotherapy%20is%20treatment,a%20large%20x%2Dray%20machine. Accessed May 3, 2021.

Wang F, Hennig J, Levan P. Time-domain principal component reconstruction (tPCR): A more efficient and stable iterative reconstruction framework for non-Cartesian functional MRI. *Magnetic Resonance in Medicine*. 2020;84(3):1321-1335.

Wang Z, Bovik A, Sheikh H, Simoncelli E. Image Quality Assessment: From Error Visibility to Structural Similarity. *IEEE Transactions on Image Processing*. 2004;13(4):600-612.

Winkel D, Bol GH, Kroon PS., et al., Adaptive radiotherapy: The Elekta Unity MR-linac concept. *Clinical and Translational Radiation Oncology*. 2019;18:54-59.

Yip E, Yun J, Wachowicz K, et al. Prior data assisted compressed sensing: A novel MR imaging strategy for real time tracking of lung tumors. *Medical Physics*. 2014;41(8):082301.

Yip E, Yun J, Wachowicz K, Gabos Z, Rathee S, Fallone BG. Sliding window prior data assisted compressed sensing for MRI tracking of lung tumors. *Medical Physics*. 2017;44(1):84-98.

Yun, J, Yip, E, Gabos, Z, Wachowicz, K, Rathee, S, Fallone, B. G. (2015). Neural-network based autocontouring algorithm for intrafractional lung-tumor tracking using Linac-MR. *Med Phys*, 42(5), 2296-2310.

Appendix A

The purpose of this appendix is to provide a numerical example in order to better understand Figure 2.3 and the process the algorithm goes through in order to fully reconstruct an image.

For this example, we will utilize a reconstruction window size of 60 frames ($N_{WIN} = 60$). This means that we will be fully reconstructing frame 60 of this window. Each frame has a resolution of 128 phase encodes by 128 read encodes. Within each frame the central 16 phase encodes will be acquired, along with all 128 read encodes for a given phase encode, in each frame in the window giving a core size of 16. From this data we will calculate the principal components. This will give us a matrix (PCA) of size 60×60 since we are acquiring principal components from 60 frames each representing a different state in the k-space evolution within the reconstruction window.

The remaining phase encodes will be undersampled in such a way that the remaining 112 phase encodes (128 phase encodes – 16 core phase encodes) are acquired in a pre-determined number of frames within the reconstruction window using complementary undersampling patterns. If we have 4 undersampling patterns ($N_{COMP} = 4$) then all of k-space will be covered every 4 frames.

We can then determine how many principal components we want to keep for use in reconstruction (N_{PC}). This number we can keep is limited to N_{WIN}/N_{COMP} principal components, in this example 60/4 = 15 principal components. An optimal value of N_{PC} using a core size of 16 and N_{COMP} equal to 4 was found to be 5 PCs. This will mean that the PCA matrix will be of size 60x5. PCA is then undersampled in a way that the columns of the undersampled matrix (PC_{US}) represent principal components calculated from frames with the same undersampling pattern. This will mean that PC_{US} will be of size 5×15.

D_{US} is a matrix which represents the acquired undersampled data, outside of the core phase encodes, of a particular undersampling pattern. It will be of size (128*112)/4×(60/5) = 3584×15. This is then multiplied by the inverse PC_{US} matrix (size 15×5). This calculates a matrix of amplitudes (A, size 3584×5) which represent how well the principal components fit to the acquired undersampled data. This amplitude matrix is multiplied by the principal components calculated from the final frame (PC_{END}) of the reconstruction window (frame 60) and again only N_{PC} principal components are kept. This gives PC_{END} a size of 5×1. The transpose of PC_{END} is

then taken. When these two matrices are multiplied some of the missing data in frame 60 is filled in. This entire process is performed (N_{COMP}-1) times in order to fill in all of the missing data. In this example the process will be performed 3 times. Once all missing data has been filled in, D_{END} is reshaped into a three-dimensional matrix of size 128×128×1. Figure A.1 provides a visual representation of this example.

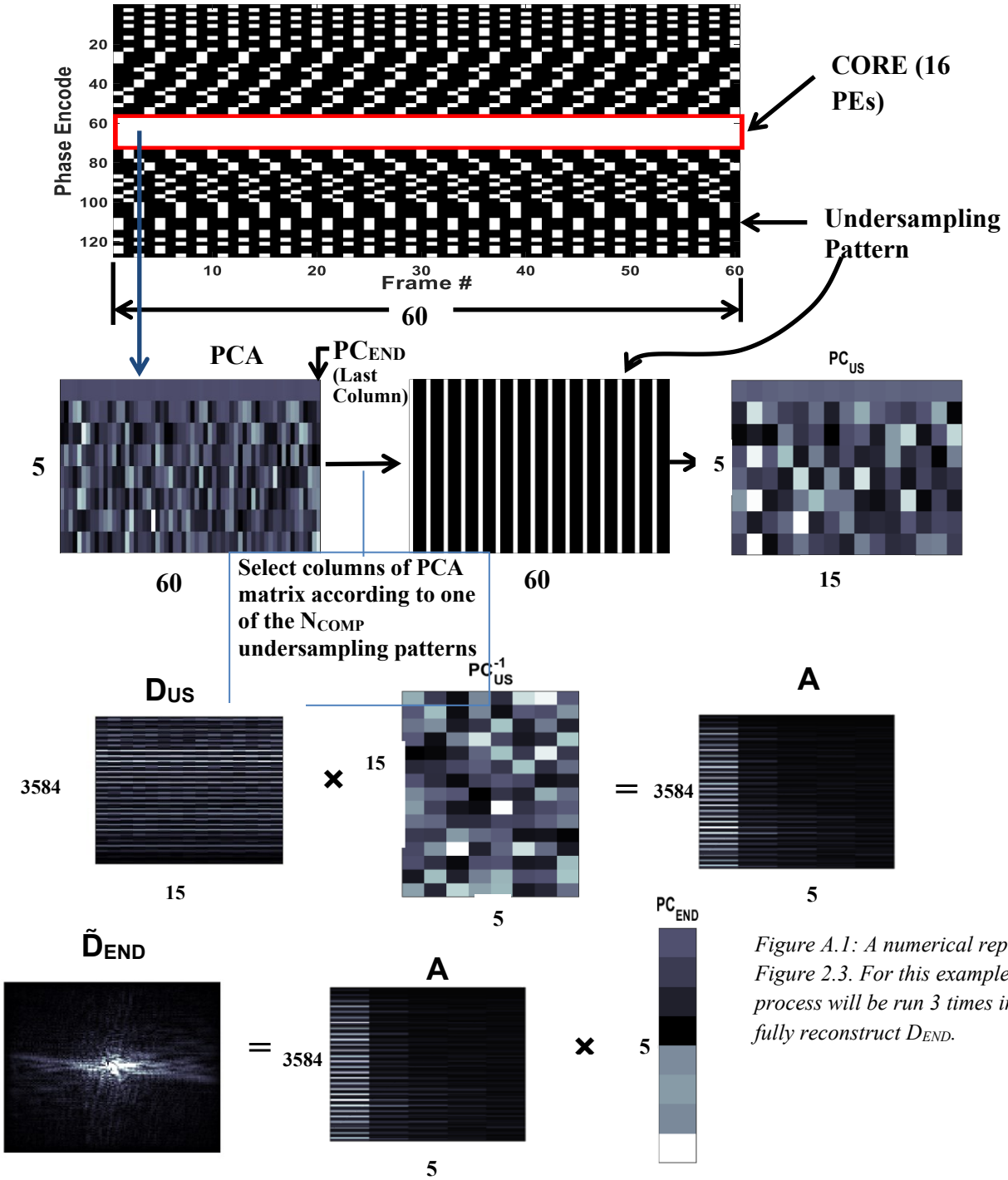

Figure A.1: A numerical representation of Figure 2.3. For this example, the entire process will be run 3 times in order to fully reconstruct D_{END}.